Spring 5-2020

Computational Imaging Methods for Analysis of DaTScan SPECT Images

Hae Sol Moon
Washington University in St. Louis

Washington University in St. Louis

McKelvey School of Engineering

Department of Biomedical Engineering

Thesis Examination Committee:
Abhinav K. Jha, Chair
Dennis Barbour
Joel Perlmutter
Richard Laforest

Computational Imaging Methods for Analysis of DaTScan SPECT Images

by

Hae Sol Moon

A thesis presented to the McKelvey School of Engineering
of Washington University in partial fulfillment of the
requirements for the degree of

Master of Science

May 2020
Saint Louis, Missouri

Contents

List of Tables . . . . . **iv**

List of Figures . . . . . **v**

Acknowledgments . . . . . **vii**

Abstract . . . . . **ix**

1 Introduction **1**
1.1 Non-invasive Brain Imaging 1
1.2 Nuclear-Medicine Imaging 2
1.2.1 Single Photon Emission Computed Tomography 4
1.3 Parkinson's Disease 6
1.3.1 Basal Ganglia 7
1.3.2 Diagnostic Techniques 10
1.4 Dopamine Transporter SPECT scans 11
1.4.1 Ioflupane 11
1.4.2 Image-Analysis-Related Challenges 12
1.4.3 Proposal 12

2 A method for DaTscan SPECT segmentation **14**
2.1 Introduction 14
2.2 Methods 17
2.2.1 Theory 17
2.2.2 Implementation 20
2.2.3 Evaluation of the proposed method 21
2.3 Results 26
2.3.1 Qualitative evaluation 26
2.3.2 Quantitative evaluation 26
2.4 Discussions 30
2.5 Conclusions 33

3 Compensating for partial volume effects in DaTscan SPECT **35**
3.1 Introduction 35
3.2 Methods 36

3.2.1 Theory for Continuous GTM Method 36
3.2.2 Evaluation of the Proposed Method 39
3.3 Results 40
3.4 Discussions and Conclusion 40

4 Conclusions and Future work 43
4.1 Overview 43
4.2 Evaluation with Physical-Phantom Study 44
4.3 Evaluation with Patient Studies 44
4.4 Performing Quantification with List-mode Data 45
4.5 Shape and Texture Analysis 45

References 47

List of Tables

3.1 The uncorrected bias and corrected bias in percentage of mean uptake values for both left and right caudate, putamen, globus pallidus and the background for DaTScan images with 2 mm voxel size are shown 40
3.2 The uncorrected bias and corrected bias in percentage of mean uptake values for both left and right caudate, putamen, globus pallidus and the background for DaTScan images with 4 mm voxel size are shown 41

List of Figures

1.1 Clinical brain SPECT scanning . . . 3
1.2 Physics of pinhole SPECT adopted from Aoi et al.[2] . . . 5
1.3 Basal ganglia . . . 8
1.4 Basal Ganglia Pathway adopted from Olanow et al., modified by Delong and Young et al.[70] . . . 9

2.1 The auto-encoder architecture for performing the segmentation of the DaTScan SPECT images. The network is input a 3D SPECT image, and outputs the estimated fractional volumes of the different regions. . . . 21
2.2 Workflow to simulate the SPECT images. DaT activity distribution map in relevant regions was attained from clinical data and structural boundaries from MR images. The digital phantom was then used for highly realistic SPECT simulation and 3D OS-EM reconstruction to generate reconstructed images. . . . 23
2.3 Visual comparison of the segmentation methods . . . 27
2.4 3D segmentation of the proposed method and comparison with the ground truth. The upper slice shows an axially upper slice and lower slice shows axially lower slice of the current slice. . . . 28
2.5 3D segmentation of the proposed method for visual comparison of normal activity and affected DaT levels where a asymmetrically reduced activity in the putamen is simulated. . . . 29
2.6 Comparison of the fDSC, fJSC, and HD from left to right respectively obtained using the five segmentation methods that allows separate segmentation for images with 2 mm voxel size (top row) and 4 mm voxel size (bottom row). . 29
2.7 The accuracy when MR and SPECT images are mis-registered. The left figure shows results with 2 mm voxel size and right figure shows results with 4 mm voxel size. . . . 30
2.8 The figure shows results with 2 mm voxel size on the left and 4 mm voxel size on the right with asymmetrically reduced functional uptake in the left and right putamen. . . . 31

3.1 (A) Original true activity distribution. (B) The spilling out effect. (C) Spilling in effect due to spilling out from (B). (D) Resulted measured image. Original figure from Soret et al. [87] . . . 36

3.2 Plot for the percent bias comparison between corrected and uncorrected results for 2 mm voxel size on the left and 4 mm voxel size on the right 41

4.1 Printed brain phantom 44
4.2 Axial DaTScan image from PPMI. Image adopted from PPMI website [64] . 45

Acknowledgments

It has been an honor working under your guidance and I would like to express my deepest gratitude to my research advisor, Professor Abhinav Jha. I have learned so many aspects of research for the last two years. His consistent and genuine enthusiasm toward computational medical imaging and teaching students have given me significant motivation for my research and studies. I am truly grateful for everything that he has done for me and the lab. Thank you so much!

I would like to thank my thesis committee members, Professor Perlmutter and Professor Laforest who I have learned very much about numerous aspects of my research through their papers and discussions.

I want to thank my undergraduate advisors, Professor Brown and Professor Pappu for their guidance and support during my studies.

When I decided in my junior year to have a career to conduct researches in brain imaging for a neurodegenerative disease, the motivation was there but I wasn't sure how to get there. I consulted with Professor Barbour who has later became my master's advisor. I engraved his advises in my mind and kept expanding my experiences and scope of knowledge. Thank you!

A special thanks goes to our lab members and great faculty within my department who have taught me many things and have supported me throughout my time at WashU.

This work was financially supported by NIH R21 EB024647 (Trailblazer award) and an NVIDIA GPU grant. We thank CHPC for providing parallel computing for this work.

Hae Sol Moon

Washington University in Saint Louis
May 2020

Dedicated to my parents.

ABSTRACT OF THE THESIS

Computational Imaging Methods for Analysis of DaTScan SPECT Images

by

Hae Sol Moon

Master of Science in Biomedical Engineering

Washington University in St. Louis, May 2020

Research Advisor: Professor Abhinav K. Jha

There is an important need to develop biomarkers to improve the diagnosis and assess the severity of Parkinson's disease (PD). The potential to derive such biomarkers from quantitative dopamine transporter scan (DaT-Scan) single-photon emission computed tomography (SPECT) imaging, in particular the uptake of DaT in the caudate, putamen, and globus pallidus regions, is highly appealing as imaging is non-invasive and DaTScan is already used in the management of patients with PD. However, reliable quantification requires reliable segmentation of these regions in these images. Reliable segmentation is challenging due to the limited spatial resolution and high image noise in SPECT images and the physiological variability in these regions. To address this issue, we propose a three-dimensional physics-guided estimation-based method for segmenting SPECT images. The method implicitly incorporates the prior distribution of boundaries of caudate, putamen and globus pallidus, as can be obtained from high-resolution MR images of patients scanned previously, during the training process. Our approach is guided by the physics of the SPECT imaging, and thus inherently accounts for the two sources of partial volume effects in SPECT images,

namely limited system resolution and tissue-fraction effects. The proposed method was evaluated both qualitatively and quantitatively using highly realistic simulation studies. The method yielded accurate boundaries of the caudate, putamen, and globus pallidus regions, provided reliable estimates of the specific binding ratios of these regions, and significantly out-performed several commonly used segmentation methods. We have implemented geometric transfer matrix (GTM) method that uses this delineated boundary to compensate for partial volume effects, with the goal of estimating more accurate quantification results.

Chapter 1

Introduction

1.1 Non-invasive Brain Imaging

The field of brain imaging stems from an effort to be able to detect and measure physical phenomena of the neural activity and biochemical reactions and properties of the brain. The brain is a especially difficult organ to image for numerous reasons. First, because there are numerous biochemical phenomena inside the brain with various yet unexplored pathways and corresponding structures and proteins, it is difficult to pin-point a specific phenomena of interest. Also, the neural connection between neurons and their cooperation are still not fundamentally understood. The presence of thick human skull makes it difficult for an imaging source such as light and sound to penetrate and lose information. Thus, an imaging device that works in small animals may not perform reliably on the human brain due to thicker and denser skull than that of small animals which creates intense attenuation for sound, light and radiation-based imaging.

Many efforts have been made to come up with imaging devices to tackle these problems and to study the brain. One of the first imaging modalities is EEG, which uses electrodes that are placed on the head of subjects to measure electrical response of neural activities. By using multiple channels, EEG provides a general understanding of spatial and temporal neuronal activity from corresponding electrical responses of the neurons. Thus, one can measure the neural activity with EEG devices and approximate the region responsible of the brain activities.

Many other efforts in imaging the brain have been conducted with the development of magnetic resonance imaging (MRI), computed tomography (CT), single photon emission computed tomography (SPECT), and positron emission tomography (PET). MRI machines use magnetic fields to measure different anatomical densities within the brain to acquire images of the brain structure. Magnetic fields are applied to the subject via coils and excite the electrons. Depending on the time constant for relaxation of tissue molecules to reach the equilibrium, MRI machines can detect such differences and allows visualization different structures within the brain. With the improvement and development of various MRI techniques such as neuromelanin sensitive MRI, fMRI and diffusion tensor MRI, researchers are able to use MRI for more specific study of interest such as imaging the structure of substantia nigra which has been a challenge with conventional T1 and T2 scans, monitor the neuronal activity level of brain regions by detecting blood flow into regions, and understand the connectivity of brain structures [82, 60, 1].

1.2 Nuclear-Medicine Imaging

Nuclear-medical imaging devices such as PET and SPECT are based on radioactive materials called radionuclides or x-rays to penetrate the bone and tissues to aid understanding of the biochemical properties at receptor sites, metabolism and functionality of specific tissue or area of body. The main imaging modalities of the brain in nuclear-medicine imaging include, SPECT and PET. For brain studies, nuclear-medicine imaging devices have widely been used due to their ability to penetrate the thick human skull which has been a challenge for many optical and sound based medical devices such as the OCT and ultrasound. In oncology, with the usage of radioactivity-labelled molecules that bind to area of metabolic activity, clinicians are able to acquire numerous information regarding the location, size and heterogeneity of the tumor. Also, nuclear-medical imaging modalities can achieve diagnostic information even at the receptor sites which made them especially useful for DA and DAT scanning for dopaminergic neurodegenerative conditions such as Parkinson's disease (PD) and dementia with Lewy bodies [98, 45].

In SPECT scanning, Anger camera rotates 360 degrees around the source of interest to acquire a 3D imaging of emitted gamma rays for about 120 angle points. Whereas in PET, the

detectors are aligned to form a circular ring around the source without rotation. PET uses positron emission which after annihilating with an electron, yields two photons in diametrically opposite directions, so that two gamma rays are detected in the detector ring from a single event. Based on the location of the detectors that are hit by the two gamma rays and with the calculation of the time difference between the two gamma rays, an approximate location of the source of gamma rays can be determined.

CT scans are widely used together with nuclear-medicine modalities such as SPECT and PET. The physics of CT scans are based on X-rays scans for 360 degrees around a subject to get numerous projection maps of the source similar to those of a SPECT system. The projection images are reconstructed for 3D image of the source by clinicians. The image acquired shows different structure of the brain depending on their ability to absorb the X-ray particles. In brain imaging, such images are used by clinicians to see the signs of head injuries and brain tumors. Also, the ability of CT scans to clearly differentiate the skull from other brain tissues allows combination of CT with SPECT or PET scans because in SPECT and PET, the information of the location of skull is important for attenuation correction due to information loss by high attenuation coefficient and the thickness of human skull [92].

Figure 1.1: Clinical brain SPECT scanning

1.2.1 Single Photon Emission Computed Tomography

Single Photon Emission Computed Tomography (SPECT) is tomographic imaging system in nuclear-medicine widely used for diverse clinical and research purposes including in oncology, cardiology, and neuroimaging. A SPECT system detects gamma rays from photon emission of radionuclide tagged tracer distributed throughout the body that is injected into the subject. The specific tracer binds to or becomes trapped by physiological properties and during the radioactive decay of radionuclide of the tracer, gamma rays are emitted. The gamma rays travel and reach the detectors of SPECT.

A SPECT systems has a unique part called collimators. The collimators are stationed in front of the detectors to allow only gamma rays that are directly parallel to the detector and reach the scintillation crystals. The scintillation crystals as a main part of the detector, transmit light when hit by gamma ray particles and the intensity of produced light gets multiplied in the photo-multiplier tube stationed after the scintillation crystals and following photosensors convert the light into electrical signal to map the projection data [13]. The detection of gamma rays, which are converted into the electrical signals, allows the mapping and thus, the understanding of biochemical properties and reactions of interest. A simple schematic of SPECT imaging starts with the injection of radio-pharmaceutical into the body of subject, uptake of such radio-pharmaceutical into the regions of interest, data acquisition of SPECT imaging, and image reconstruction/analysis.

SPECT Simulations

In order to conduct studies in economically and timely efficient manner, in numerous SPECT research studies, prior to testing on a clinical SPECT scanner, computerized simulations of SPECT imaging are used. This allows more freedom in experimenting with numerous parameters and techniques to acquire ideal SPECT setting on computers. Simulations also allow modeling population variability. However, in order to achieve a highly realistic simulations, SPECT physics processes have to be incorporated mathematically such as collimator-detector response, attenuation and scatter in both simulations and reconstruction protocols [59]. Especially, the collimator and detector determine resolution of the system. The collimator also

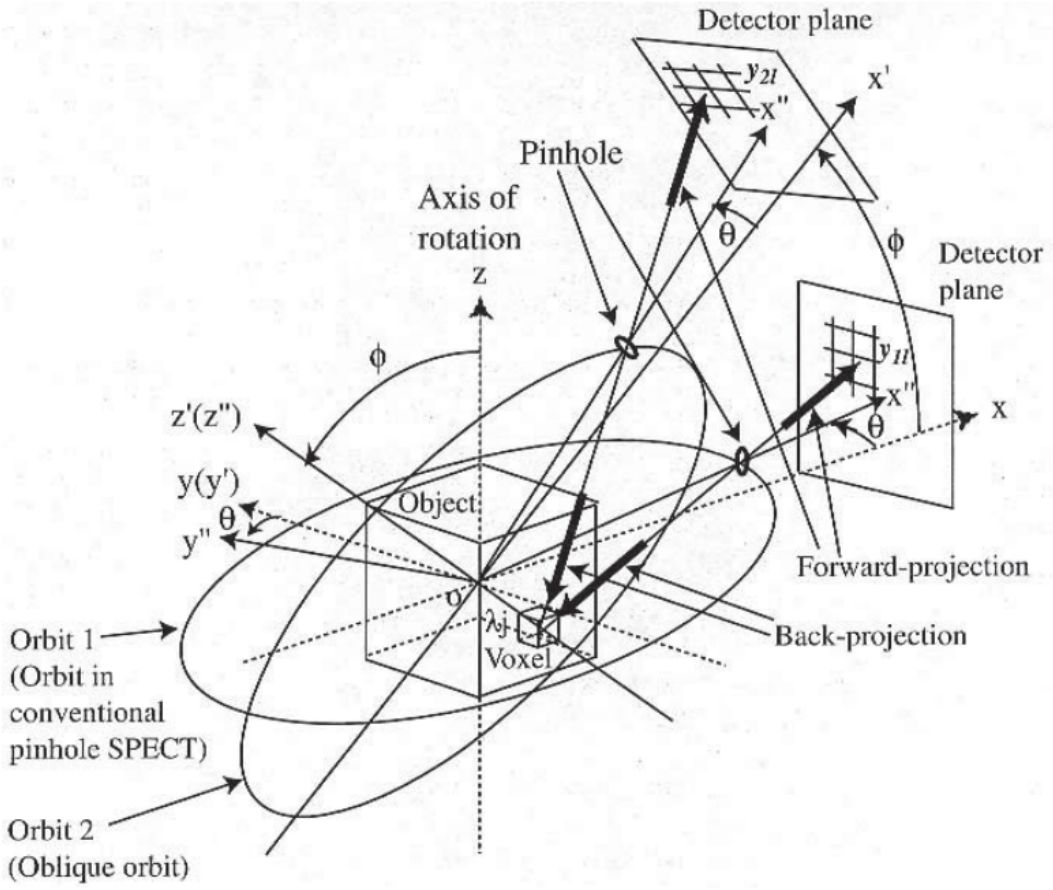

Figure 1.2: Physics of pinhole SPECT adopted from Aoi et al.[2]

determines the sensitivity of a SPECT scanner. The factors that affect collimator resolution include distance from the source to collimator, hole size, and hole shape. Typically, low energy and high resolution collimators (LEHR) are used for DatScan studies and has around 7.4 mm FWHM at 10 cm [86]. Further, scintillating crystals and photo-multiplier tube determine the intrinsic resolution. Intrinsic resolution varies between SPECT scanners but generally is around 4 mm FWHM [86].

The mathematical modeling of the deterministic portion of any imaging system can be expressed through the formalism g=Hf, where f is the object that is being imaged, and g is the acquired data from the imaging system. H represents the system response and the behavior of the imaging system and in a linear discrete-to-discrete system, can be expressed in a matrix form, also referred to as the system matrix. In order for a simulation method

to be realistic, it is important to take into accounts of various SPECT imaging physics and to achieve a reliable digital phantom of the uptake distribution depending on the type of isotope used in the study.

SPECT Reconstruction

After acquiring the H matrix, an iterative reconstruction method namely maximum likelihood-expectation maximum (ML-EM) and ordered subset-expectation maximum methods are used for reconstruction (OS-EM) [51, 28]. The method computes the ratio between measured and estimated projection and the back projection of the ratio will be multiplied to previous iteration of estimated image to generate image of new iteration. The difference between measured and estimated projection will be incorporated into each iteration and after a specific iteration, theoretical and measured image will become similar. Thus, it is highly important to achieve a highly realistic H matrix that incorporates the realistic nature of a SPECT system configuration into account.

In each iteration of ML-EM, an updated reconstructed image can be explained and mathematically expressed as follows:

$$Image^{(k+1)} = Image^{(k)} \times Normalized\ Backprojection\ of\ [\frac{measured\ projection}{estimated\ projection^{(k)}}] \quad (1.1)$$

$$\bar{f}_n^{(k+1)} = \frac{\bar{f}_n^{(k)}}{\sum_{m'=1}^{M} H_{m'n}} \sum_{m=1}^{M} \frac{g_m}{\sum_{n'=1}^{N} H_{mn'} \bar{f}_{n'}^{(k)}} H_{mn} \quad (1.2)$$

1.3 Parkinson's Disease

Neurodegenerative disorders are characterized by irreversible degeneration of neuronal cells that deteriorates various functionalities of the brain including cognitive abilities. Parkinson's disease is the second most common neurodegenerative disease after Alzheimer's [19, 63]. The diagnostic symptoms of PD are rigidity, bradykinesia, akinesia, abnormal posture and resting tremor [62]. Bradykinesia is the slowing of muscle movement and akinesia represents the loss

of voluntary muscle movement. Ridgitity refers to stiffness of the muscle. These symptoms occur due to the inability of the PD patients to relax undesired muscle contraction. Also, tremor is one of the most commonly associated with patients with PD. A tremor refers to a rhythmic, oscillating and involuntary movement or shake that occurs in the body [85]. This behavior also occurs in other motor-related illnesses such as essential tremor, a neurological disease that causes involuntary tremor when trying to move muscle. However, in PD, tremor occurs in a resting state, which is known as resting tremor that occurs even when the patients are at rest. The resting tremor not only occurs in fingers and large muscles such as foot, hand, leg or arm but also lips, jaw and tongue [30]. The symptoms that are related to motor functions such as muscle control, balance and movement can be explained by the neuronal loss in the substantia nigra where most of the dopamine neurons are located, as will be explained more in detail.

Further, non-motor symptoms such as depression, apathy, sleep disorders and erectile dysfunction are known to occur in patients with PD [6]. It is still unclear the exact pathway and the cause of such neurodegeneration in PD. In most cases, the diagnosis of PD occurs after about 50% of dopamine neurons have already been lost [12]. Also, PD is sometimes misdiagnosed and an accurate diagnosis is challenging [12].

1.3.1 Basal Ganglia

Direct Pathway

Basal Ganglia is a group of structures that includes caudate, putamen, globus pallidus and midbrain that takes a crucial role in the neuronal circuit of the brain. The basal ganglia is connected to the motor cortex and the thalamus through inhibitory and excitatory synapses with GABA and glutamate as neurotransmitters. In a voluntary movement, when a person tries to move, the motor cortex sends an excitatory signal with the release of glutamates into the striatum which then inhibits globus pallidus internal (GPi) as the striatum releases GABA. When GPi is inhibited, the normal inhibitory effect on the the thalamus is also inhibited which in turn, excites the thalamus. Then, the excited thalamus sends excitatory signal to the motor cortex and excites the muscles for movement.

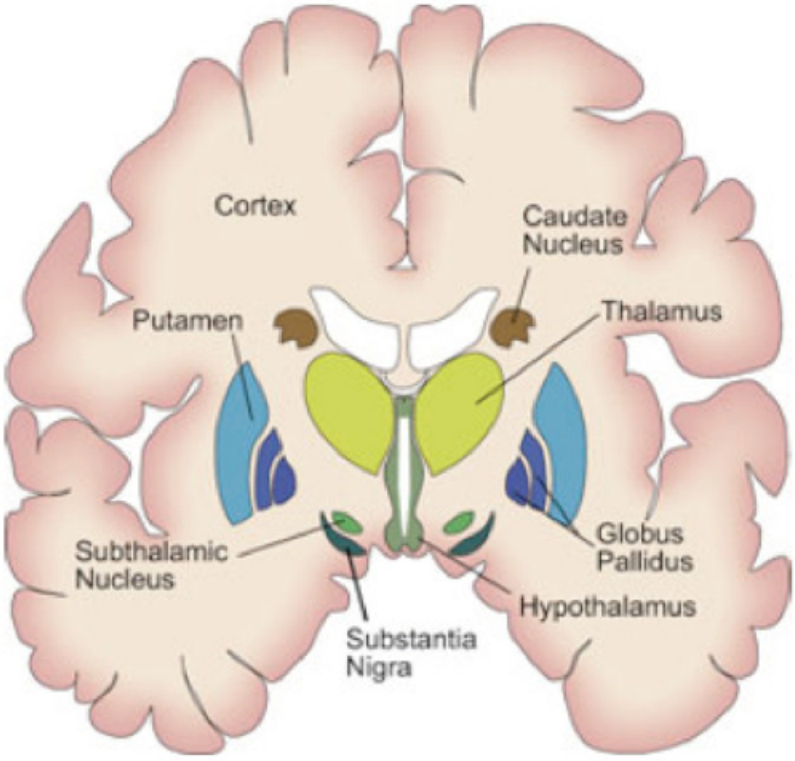

Figure 1.3: Basal ganglia

The substantia nigra has a regulatory role in the direct pathway. The striatum contains D1 dopamine receptors that receive dopamine from substantia nigra. The substantia nigra connects with the inhibitory neurons from striatum and globus pallidus through dopaminergic neurons in the niagrostriatal pathway. When striatum receives dopamine from substantia nigra, GPi is more inhibited leading to amplified effect in the direct pathway. Such response is regulated with the amount of dopamine transported from the substantia nigra to the striatum.

Indirect Pathway

The indirect pathway of muscle movement mainly occurs to prevent undesirable movement by inhibiting the execution of thalamus which excites the motor cortex. GPi controls the thalamus by inhibiting thalamus. Also, the motor cortex excites the striatum and inhibits

globus pallidus external (GPe), which then inhibits the connection with subthalamic nucleus. This results in excited subthalamic nucleus that sends excitatory messages to GPi which inhibits the activity of thalamus by sending out more GABA neurotransmitters. Then, thalamus sends less excitatory signal to the motor cortex and leads to a decreased muscle movement. The substantia nigra also plays an important role in the indirect pathway as a regulator. The substantia nigra sends dopamine which binds to D2 receptors in the striatum. With the increase of dopamine binding to D2 receptors results in less inhibitory response to GPe from the striatum in the indirect pathway. The level of dopamine controls the response of thalamus leading to either increased or decreased muscle movement.

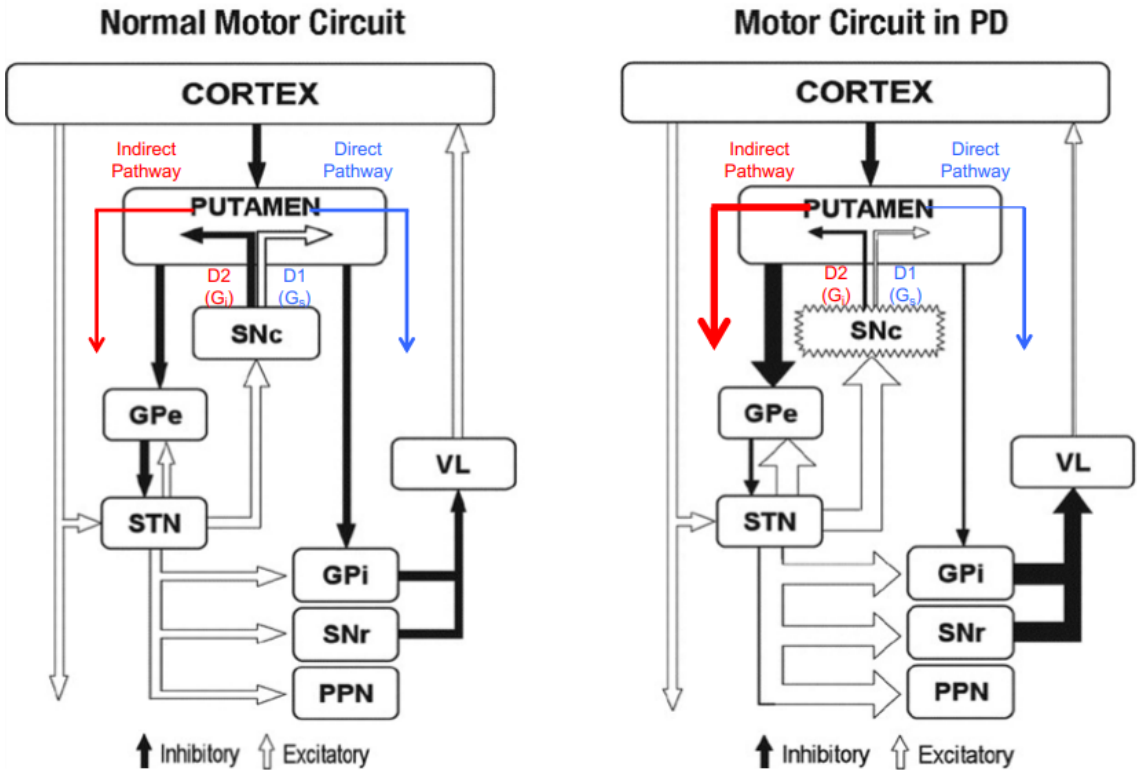

Figure 1.4: Basal Ganglia Pathway adopted from Olanow et al., modified by Delong and Young et al.[70]

What Happens in Parkinson's Disease?

In PD, dopaminergic neurons in the nigrostriatal pathway which connects the substantia nigra and striatum dies due to unknown causes. Similar to Lewy body dementia, in PD,

there exists an accumulation of abnormal protein bundles called Lewy bodies which form in the substantia nigra [88]. As the dopaminergic neurons die, less dopamine is transported from the substantia nigra to the striatum that effects both direct and indirect pathway of muscle movement. In the direct pathway, the goal is to excite thalamus to induce muscle movement. However, in PD, due to loss of dopaminergic neurons leading to decreased levels in the striatum, the thalamus is less activated which leads to reduced muscle movement. In the indirect pathway, as dopamine levels decrease in the striatum, the "fine-tuning" ability of substantia nigra as a regulator of muscle movement is reduced. Thus, the loss of dopaminergic neurons leads to less dopamine movement from substantia nigra to striatum and causes loss of the ability to trigger extensive muscle movement and to prevent excessive movement evident from slow movement and resting tremors of patient's with PD.

Also, there is an increasing need for clinical investigation of globus pallidus in PD [52, 53, 9, 8, 79]. There has been an observed correlation between DaT reduction in globus pallidus and resting tremor severity which is one of the distinct symptoms of PD [26]. Studies have found an increase in F-dopa uptake in GPi in early stages of PD [100]. The authors hypothesized that the uptake in GPi was increased to maintain a more normal pattern of pallidal output to ventral thalamus and motor cortex to compensate for the early degeneration of nigrostriatal dopaminergic neurons. As the disease progressed, uptakes in GPi then gradually decreased. The authors suggested that the loss of this pathway in PD may be an important step in the progression of the disease. These findings bring significant interest in quantifying uptake in globus pallidus.

1.3.2 Diagnostic Techniques

UK PD Society Brain Bank Criteria

The UK PD society brain bank criteria is a widely used clinical diagnostic criteria for PD developed by PD society brain bank (PDSBB) in London [29]. The criteria begins with the diagnosis of Parkinsonian Syndrome with bradykinesia, and presence of at least one of muscular rigidity, 4-6 Hz of rest tremor and postural instability not caused by primary visual, vestibular, cerebellar or proprioceptive dysfunction [29]. Next step is to perform exclusion criteria for PD which includes history of repeated strokes, head injury, more than

one affected relative, presence of cerebral tumor, exposure from MPTP and more [29]. The final step is the supportive prospective positive criteria for PD. Three or more of the last criteria step are required for a diagnosis of definite PD as well as the check for the first step which includes, unilateral onset, presence of rest tremor, disorder progression, asymmetry of affected side, 70-100 % response to L-Dopa, severe L-Dopa induced chorea and a response from longitudinal study [29].

United PD Rating Scale

The united PD rating scale (UPDRS) is a scaling system that rates the severity of PD based on symptoms which ranges from 0 to 199 maximum points. The UPDRS has four parts including non-motor experiences of daily living, motor experiences of daily living, motor examination and motor complications [23]. The first part includes psychological symptoms such as cognitive impairment and hallucination and in part two, motor symptoms including handwriting and tremors and speech are examined [23]. The first two parts are performed through an interview with a physician, part three is a structured physical examination for motor performance and the last section is performed through interview and observation [23].

1.4 Dopamine Transporter SPECT scans

1.4.1 Ioflupane

The loss of dopaminergic neurons is one of the main symptoms of PD. Thus, it is compelling to investigate metrics that can show the changes of dopaminergic neurons as biomarkers. Ioflupane (I-123) is a radionuclide that is a cocaine analogue. Cocaine analogues have a high affinity to dopamine transporters in the presynaptic terminal of dopaminergic neurons especially found in the striatum [5, 83]. The affinity of I-123 to dopamine receptors depends on the availability of DaT in the presynaptic terminal which is affected by the severity of PD. Thus, patients with severe PD will have reduced DaT uptake in the striatum region and that will be largely asymmetric. Radiologists visually assess SPECT scans as one of the criteria of the differential diagnosis.

1.4.2 Image-Analysis-Related Challenges

Various segmentation methods in medical imaging have been developed for numerous purposes. Such methods serve the goal of extracting region of interest such as tumors or lesions. Also, in MRI images, segmentation methods have been developed to delineate various structures of the brain. This is made possible by relatively higher resolution and lower noise levels of MRI images of the brain. A program called Freesurfer is used in this study to segment T1 MRI images into various regions of the brain such as caudate, putamen, globus pallidus, grey matter and white matter [20]. However, in nuclear-medicine imaging and especially in SPECT scans, images are largely distorted due to partial volume effects resulted from high noise and low resolution of imaging systems. Thus, conventional intensity-based segmentation methods of SPECT images such as thresholding, gradient-based and MRF-GMM suffer from low segmentation accuracy because the shape difference between an actual structure of region of interest and visual shape in SPECT images are quite different. There have been numerous studies to determine a quantitative biomarker for PD through DaTscan SPECT but a reliable early detection method and a biomarker that correlates with the progression and severity of PD have yet to be developed. In many studies, simpler and less accurate segmentation methods such as thresholding were used and more focus was on the analysis aspect instead of the segmentation accuracy. Thus, there is a need for a segmentation method that accounts for PVEs and a quantification method that also accounts for PVEs. This study focuses on both aspects of these problems to achieve the goal of accurate quantification that largely corrects PVEs. In our study, we focus on achieving accurate segmentations and use those segmentations to develop a quantitative biomarker for assessing mean uptake in regions of interest.

1.4.3 Proposal

We propose to address the challenges with analysis of DaTscan SPECT images through the development of new image analysis methods. In this thesis, we focus on developing and evaluating these tools in the context of analyzing the caudate, putamen, and globus pallidus regions thus, developing a robust quantification metric for in vivo phenomena. We are interested in quantifying the uptake in globus pallidus along with widely studied caudate

and putamen to investigate the correlation between uptake in globus pallidus and the severity of PD as well as to advance understanding of pathological role of globus pallidus in PD [26, 52, 53, 9, 8, 79, 100]. In clinical trials [101, 78, 22, 16, 50], including the seminal ELLDOPA study [24] and MPTP-treated non-human primate studies [96, 42, 94], striatal measures did not fully correlate with the severity of PD, thus limiting the effectiveness of only using striatal uptake as a biomarker to measure or predict the progression of PD. Thus, a combined analysis of caudate, putamen and globus pallidus, may provide useful information that hasn't been explored yet. We first propose a new estimation-based approach to SPECT segmentation that integrates the physics of SPECT imaging with a learning-based approach. We observe that the proposed method yields accurate segmentations of the caudate, putamen, and globus pallidus in brain SPECT images, as evaluated using realistic simulation studies. The method is described in Chapter 2. In Chapter 3, a PVC method is developed to address the issues of PVEs in quantification. This approach builds upon an approach initially proposed in Du et al. and demonstrates promise in the task of PVC from SPECT images. In summary, this thesis seeks to develop tools to address the challenges of segmentation and PVC in DaTscan SPECT images, specifically in the context of performing reliable quantification from the caudate, putamen, and globus pallidus regions of the brain.

Chapter 2

A physics-guided learning-based estimation method for fully automated 3D DaT-Scan SPECT segmentation[1]

2.1 Introduction

Parkinson's disease (PD) is the second-most common neurodegenerative disease after Alzheimer's disease and is estimated to affect 12 million people worldwide by 2040 [19, 63]. Dopamine transporter (DaT) SPECT scans are conducted to improve diagnosis, and more specifically, to separate PD from other Parkinsonian syndromes such as Essential Tremor [83]. For this purpose, conventionally, DaTscan images are analyzed visually. However, several studies are investigating whether quantitative uptakes in the striatal regions, i.e. the caudate and the putamen, can help with more accurate diagnosis [40]. Also, there is significant interest in using quantitative DaT SPECT-derived measures for measuring disease severity in patients with PD [53, 52, 77]. Moreover, studies have shown evidence of DaT in globus pallidus (GP) [8, 75] and its correlation to motor severity and progress of PD [53]. For all these studies, there is a need for methods to quantify regional DaT uptakes from SPECT

[1]This chapter forms the basis of an article that will be submitted to a journal. Authors include Hae Sol Moon, Ziping Liu, Richard Laforest, Maria Ponisio and Abhinav K. Jha. Abstracts based on this work have been accepted to the IEEE International Symposium on Biomedical Imaging 2020 and the Society of Nuclear Medicine and Molecular Imaging Annual Meeting 2020

images. Additionally, there is substantial interest in using shape analysis of the caudate and putamen boundaries to develop biomarkers for PD [89, 76]. Further, texture analysis of DaTscan images is also being explored [65, 3]. Conducting these quantification, shape and texture-analysis studies requires reliable segmentation of the caudate, putamen, and GP regions from DaT-scan SPECT images.

Segmentation in SPECT is challenging in general due to the low resolution and resultant partial-volume effects (PVEs, high noise and physiological variability between subjects [4, 14]. The problem is further compounded in DaTscan SPECT because of the small sizes of the caudate, putamen, and GP regions. In fact, the GP is visually almost impossible to demarcate from SPECT images. The commonly used segmentation procedure for SPECT is manual delineation by trained readers. However, manual delineation is expensive, tedious, time consuming, and suffers from intra-and inter-reader variability, especially due to the poor resolution and high noise in SPECT [33]. To address this issue, several semi-automated SPECT segmentation methods have been proposed, such as those based on thresholding [61, 97], edge-detection [61], region-growing [84], and clustering [68]. However, our studies show that these methods yield limited performance when applied to DaT-scan SPECT. This was primarily due to the lack of clear boundaries and the relatively low tracer uptake in the GP region. Often times these existing methods segmented the caudate, putamen and GP as just one unified region, which limits the ability to quantify regional uptakes from these regions. A recent study showed that metrics measured from DaTscan SPECT after applying a semi-automated segmentation method yielded large variabilities, and thus were clinically not useful [66]. Thus, there remains an important need for improved methods to segment DaTScan brain SPECT images.

To address this need, we recognize that a major barrier to segment DaTscan SPECT images into caudate, putamen, and GP is the lack of clear boundaries between these regions in these images. This arises due to the PVEs in reconstructed SPECT scans. These PVEs have two sources: limited system resolution and tissue-fraction effects (TFEs). Clinical brain SPECT systems typically have resolution of the order of ~ 8 mm, and following reconstruction, the resolution in the reconstructed image can be around ~ 12 mm. [90, 10] Thus, structures such as caudate, putamen and GP, which are close to each other, are significantly affected by the system-generated blur. Further, due to reconstruction of the image over a finite-sized voxel grid, it is likely that a voxel contains more than one region. While this is generally an issue

in medical imaging, the effect is more prominent in SPECT due to the larger reconstructed voxel sizes.

Conventional segmentation methods are designed as classifiers, in that they classify a voxel as belonging to a certain region. Thus, they are inherently unable to account for the TFEs. To address this issue in the context of segmenting oncological 2-D PET images, Liu et al. [58, 57] have proposed an estimation-based segmentation method. The method instead of classifying a pixel as tumor or background, estimates the fractional area that the tumor occupies within each pixel. We now propose to extend this technique in the context of segmenting multiple regions, namely the left and right caudate, putamen and GP, from 3-D SPECT images. The estimation-based segmentation technique is a Bayesian approach, and as shown later, requires a distribution of the fractional volumes that the caudate, putamen, and GP regions occupy in each voxel. To obtain this distribution, we use the fact that these regions are separately visible on T1-weighted MR images, where they can be easily delineated. Since the T1-weighted MR images are anatomical, this provides the anatomical fractional volumes in each voxel for the different regions. The proposed method uses this distribution to estimate the posterior mean of the fractional volumes of the caudate, putamen, and GP regions from the DaT-scan SPECT images. These estimates yield the segmentations of these regions over a continuous non-voxelized grid, analogous to segmentation of a high-resolution image.

This paper is organized in the following sections. In Section 2.2, we provide the theoretical formalism, implementation, and evaluation of the proposed method. An important component of the evaluation study is investigating the performance of the method when there is a mismatch between the distribution learned from the MR image population and the SPECT image. We investigate the sensitivity of the method to these mismatches. The results are presented in Sec. 2.3. Finally, the implications of the results along with limitations and future directions are presented in Sec. 2.4, followed by the conclusions in Sec. 2.5.

2.2 Methods

2.2.1 Theory

Problem formulation

Let $f(\mathbf{r})$ describe the DaT tracer distribution within the brain for a patient injected with this tracer, where $\mathbf{r}$ is a 3D vector denoting spatial location. Consider a SPECT system that images this 3D tracer distribution and yields sinogram data. The sinogram data is input to a reconstruction method, yielding a reconstructed image $\hat{\mathbf{f}}$ consisting of M voxels. Denote the process of obtaining the reconstructed image from the original tracer distribution by the operator $\Theta : \mathbb{L}_2(\mathbb{R}^3) \rightarrow \mathbb{E}^M$. Our objective is to segment the reconstructed image into K regions, in this case, the left and right caudate, putamen, and GP regions, with the rest of the region labeled as the background. Typically this is performed by labeling each voxel in the reconstructed image to one region. However, as mentioned above, this segmentation is unable to account for tissue-fraction effects. Thus, we instead frame the segmentation problem as estimating the fractional volume occupied by the k^{th} region in each voxel of the reconstructed image $\hat{\mathbf{f}}$.

Let the support of the k^{th} region be given by $\phi_k(\mathbf{r})$. Mathematically,

$$\phi_k(\mathbf{r}) = \begin{cases} 1, & \text{if region } k \text{ occupies location } \mathbf{r}. \\ 0, & \text{otherwise.} \end{cases} \tag{2.1}$$

Also, let the distribution of tracer uptake within the support of each region be given by $f_k(\mathbf{r})$. Then $f(\mathbf{r})$ can be described as follows:

$$f(\mathbf{r}) = \sum_{k=1}^{K} f_k(\mathbf{r})\phi_k(\mathbf{r}). \tag{2.2}$$

Next, define the voxel function $\psi_m(\mathbf{r})$ as

$$\psi_m(\mathbf{r}) = \begin{cases} 1, & \text{if } \mathbf{r} \text{ lies within the } m^{\text{th}} \text{ voxel.} \\ 0, & \text{otherwise.} \end{cases} \tag{2.3}$$

Let V denote the total volume of each voxel. The fractional volume occupied by the k^{th} region in the m^{th} voxel, denoted by $v_{\text{ideal},k,m}$, is given by

$$v_{\text{ideal},k,m} = \frac{1}{V} \int \phi_k(\mathbf{r}) \psi_m(\mathbf{r}) d^3\mathbf{r}. \tag{2.4}$$

Estimating the fractional volumes within each voxel thus requires estimating the values of $\phi_k(\mathbf{r})$ from $\hat{\mathbf{f}}$. This is an ill-posed problem due to the null functions of the Θ operator. One way to alleviate the ill-posedness is to incorporate prior distribution about $\phi_k(\mathbf{r})$. However, this requires access to the distribution of $f(\mathbf{r})$, or at least $\phi_k(\mathbf{r})$, at infinitely high resolution. Liu et al. [58] proposed a simulation-based strategy for this purpose, where in the context of oncological PET, they simulated tumors at very high resolution. However, their strategy required simulating tumors and then validating their realism.

In our problem, we benefit from the availability of existing MR image populations, which can be used to provide the distribution of $\phi_k(\mathbf{r})$ at relatively higher resolution. More specifically, the anatomical structures of the caudate, putamen and GP regions are distinguishable on MR images due to the higher resolution of MRI. The MR images can thus be segmented to yield the support of these regions. Thus, from previously acquired MR images, a distribution of the support of these regions can be obtained.

Denote the MR image by an N-dimensional vector $\mathbf{f}_{MR}$, where $N > M$. The voxel function for this image is denoted as $\psi_m^{MR}(\mathbf{r})$. Assume that this image has been segmented into K distinct regions. For each region, we define a N-dimensional vector $\boldsymbol{\phi}_k^{MR}$, which denotes the mask for that region. The elements of this vector are defined as follows:

$$\phi_{k,i}^{MR} = \begin{cases} 1, & \text{if voxel } i \text{ in the MR images is assigned to region } k. \\ 0, & \text{otherwise.} \end{cases} \tag{2.5}$$

A high-resolution estimate of the fractional volume occupied by the k^{th} region in the m^{th} voxel of the SPECT image, denoted by $v_{k,m}$, is then given by

$$v_{k,m} = \frac{1}{V} \sum_{m'=1}^{M} \phi_{k,m'}^{MR} \int d^3r \; \psi_{m'}^{MR}(\mathbf{r}) \psi_m(\mathbf{r}). \tag{2.6}$$

We frame our problem as the task of estimating $\{v_{k,m}, k = 1, 2, \ldots K, m = 1, 2, \ldots M\}$ from the reconstructed SPECT images.

Estimation technique

Denote the estimate of $v_{k,m}$ by $\hat{v}_{k,m}$. Denote the vector $\{v_{k,m}, m = 1, 2, \ldots M\}$ by $\mathbf{v}_k$, and the estimate of $\mathbf{v}_k$ by $\hat{\mathbf{v}}_k$. To compute $\hat{\mathbf{v}}_k$ from the reconstructed SPECT image $\hat{\mathbf{f}}$, we first need to define a cost function. The values of $v_{k,m}$ and $\hat{v}_{k,m}$ lie between 0 and 1. Thus, if we treat these values as probabilities, the binary cross entropy (BCE) between $v_{k,m}$ and $\hat{v}_{k,m}$ automatically incorporates this constraint on the range of these values [11]. Therefore, the BCE loss, denoted by $l_{\text{BCE}}(v_{k,m}, \hat{v}_{k,m})$, and given by the equation below is chosen as the basis of the cost function:

$$l_{\text{BCE}}(v_{k,m}, \hat{v}_{k,m}) = v_{k,m} \log(\hat{v}_{k,m}) + (1 - v_{k,m}) \log(1 - \hat{v}_{k,m}). \tag{2.7}$$

The cost function, denoted by $C(\mathbf{v}_k, \hat{\mathbf{v}}_k)$, minimizes the negative of the BCE loss between $v_{k,m}$ and $\hat{v}_{k,m}$ over all M voxels, averaged over the ensemble of true values $v_{k,m}$ and the noise in the imaging process. The cost function is then given by:

$$C(\mathbf{v}_k, \hat{\mathbf{v}}_k) = -\sum_{m=1}^{M} \int \int \; \mathrm{p}(\hat{\mathbf{f}}, v_{k,m}) l_{\text{BCE}}(v_{k,m}, \hat{v}_{k,m}) dv_{k,m} d^M \hat{f}. \tag{2.8}$$

We use Bayes theorem to expand $\mathrm{p}(\hat{\mathbf{f}}, v_{k,m})$ and replace the expression from Eq. (2.7) in the cost function (Eq. (2.8). This yields:

$$\begin{aligned} C(\mathbf{v}_k, \hat{\mathbf{v}}_k) &= -\sum_{m=1}^{M} \int \mathrm{p}(\hat{\mathbf{f}}) \int \mathrm{p}(v_{k,m}|\hat{\mathbf{f}}) \left[v_{k,m} \log(\hat{v}_{k,m}) + (1 - v_{k,m}) \log(1 - \hat{v}_{k,m}) \right] dv_{k,m} d^M \hat{f} \\ &= -\sum_{m=1}^{M} \int \mathrm{p}(\hat{\mathbf{f}}) \int \mathrm{p}(v_{k,m}|\hat{\mathbf{f}}) \left[v_{k,m} \{ \log(\hat{v}_{k,m}) - \log(1 - \hat{v}_{k,m}) \} + \log(1 - \hat{v}_{k,m}) \right] dv_{k,m} d^M \hat{f} \\ &= \sum_{m=1}^{M} \int \mathrm{p}(\hat{\mathbf{f}}) \left[\{ \log(\hat{v}_{k,m}) - \log(1 - \hat{v}_{k,m}) \} \int \mathrm{p}(v_{k,m}|\hat{\mathbf{f}}) v_{k,m} dv_{k,m} + \log(1 - \hat{v}_{k,m}) \right] d^M \hat{f}. \end{aligned} \tag{2.9}$$

The term $\mathrm{p}(\hat{\mathbf{f}})$ is always positive. Thus, the cost function is minimized by setting

$$\frac{\partial}{\partial \hat{v}_k, m} \left[\{ \log(\hat{v}_{k,m}) - \log(1 - \hat{v}_{k,m}) \} \int \mathrm{p}(v_{k,m}|\hat{\mathbf{f}}) v_{k,m} dv_{k,m} + \log(1 - \hat{v}_{k,m}) \right] = 0. \tag{2.10}$$

The solution is given by

$$\hat{v}^*_{k,m} = \int \mathrm{p}(v_{k,m}|\hat{\mathbf{f}}) v_{k,m} dv_{k,m}. \tag{2.11}$$

This is simply the posterior mean estimate of $v_{k,m}$. Thus, by developing an optimization routine that minimizes the loss function in Eq. (2.7), we can estimate the fractional volume that a region occupies in each voxel. From this estimate, the segmented boundaries of the different regions can be obtained, as we define later. We first describe the procedure to develop such an optimizer.

2.2.2 Implementation

An encoder-decoder-based architecture was implemented to minimize the cost function defined in Eq. (2.7). The auto-encoder was input the 3D SPECT images and corresponding ground-truth masks for training. On being trained, the network, when input a 3D SPECT image, estimates the fractional volumes of the of left and right caudate, putamen and GP, which are then used to define the 3D delineations of these regions. The network architecture

is shown in Fig. 2.1. The architecture is similar to a modified U-net as proposed in Leung et al. [54], but with some differences. The major difference is that the argmax layer is not present. This allows the network to output a continuous valued estimate of the fractional volume within each voxel, as a number between 0 and 1. This network design is similar to other networks that are designed for estimation-based tasks, such as those for denoising [11] and reconstruction [69]. The detailed architecture is shown in Appendix A. We implemented this approach in 3D instead of conducting slice-by-slice segmentation or patch-based training [41] to provide the maximal amount of global contextual information per patient image.

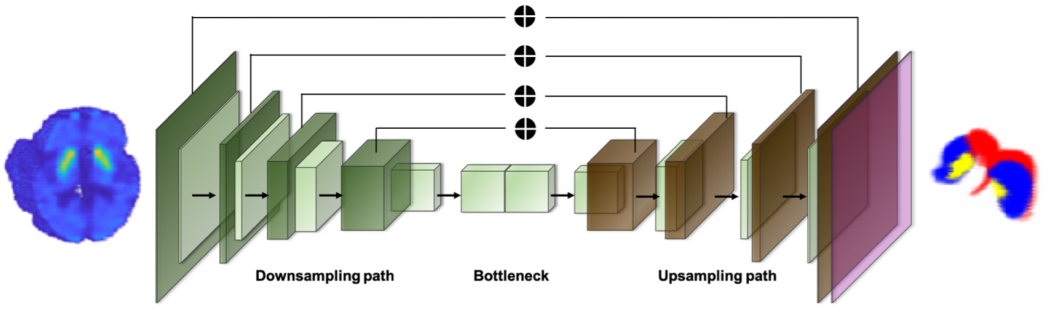

Figure 2.1: The auto-encoder architecture for performing the segmentation of the DaTScan SPECT images. The network is input a 3D SPECT image, and outputs the estimated fractional volumes of the different regions.

The method was implemented on systems with NVIDIA Titan RTX GPU and NVIDIA V100 graphics processing unit (GPU) cards, allowing effective training with 3D images. Tensorflow 1.10.0 was used with Keras. Also, Python 3.7 programming language was used.

2.2.3 Evaluation of the proposed method

Evaluation of the proposed method requires access to DaT-scan SPECT images where the ground-truth boundaries of the various regions are known. One approach to conduct such a study is to have ground-truth boundaries defined by expert readers. However, this approach is likely erroneous with SPECT as the manual delineations are not guaranteed to be accurate due to the PVEs in SPECT. In fact, the GP is manually almost impossible to delineate on the SPECT scan. Further, the boundary between the caudate and putamen is unclear. All these factors make obtaining manual delineations nonviable. Another evaluation approach is

a setup where both the MR and DaT-scan SPECT images for a certain set of patients were acquired. However, such images are difficult to obtain due to the lack of joint SPECT/MR systems. In some cases, SPECT and MR images from different scanners may be available. However, using these images requires assuming that the MR and SPECT scans are perfectly aligned, which is not guaranteed. Further, this approach assumes similarity of the functional boundary on the SPECT and the anatomical boundary on the MR image.

To address these issues, we perform this evaluation in a more controlled setting through realistic clinically guided simulation studies where the above-mentioned assumptions do not need to be made. In these studies, clinical MR images are used to generate clinically realistic SPECT images by modeling the physics of SPECT. This process inherently ensures that the MR-defined ground-truth boundaries of the various regions in the generated SPECT images are known and that the images are aligned perfectly. Further, this approach allows us to precisely and quantitatively study the effects of misalignment between the SPECT and MR images, and the mismatch between the MR functional and SPECT anatomical boundaries. Note that while this strategy requires simulation of SPECT system, the true distribution of the fractional volumes of the different regions is not simulated and is obtained directly from clinical studies. In this section, we describe the process followed to rigorously evaluate the proposed method using this simulation-based approach.

Generating realistic SPECT images

A total of 600 T1-weighted MR images from the Open Access Series of Imaging Studies (OASIS)-3 [48] and Alzheimer's Disease Neuroimaging Initiative (ADNI) [74] databases were used. These images were segmented into grey matter, white matter, caudate, putamen and GP for both left and right hemispheres using the Freesurfer software. The delineation was performed in Montreal Neurological Institute (MNI) space into $256 \times 256 \times 256$ voxels with voxel size of 1 mm. The resulting delineations of MR images yielded 600 anatomical templates of the brain. Next, an *in vivo* distribution of DaT activity ratios in the different regions of the brain, as obtained from clinical data in Lee et al. [53], was defined. For each anatomical template, this distribution was sampled to determine the DaT activity ratios in the various regions. This process ensured clinically realistic variability of activity uptake for the different subjects. At the end of this process, we had a digital phantom population

of 600 patients with anatomical templates directly obtained from clinical data and tracer distributions guided by clinical data.

This ground-truth tracer distribution was used to generate realistic DaT-scan SPECT images. A SPECT system modeling a DaT-scan study with 123-Ioflupane tracer and a low-energy high-resolution (LEHR) collimator was simulated. System parameters were similar to a GE Discovery 670 (GE Healthcare, Haifa, Israel). The simulation process modeled the various aspects of SPECT imaging, including the finite extent of the collimator, the finite energy and spatial resolution of the detectors and the photon attenuation. The number of total counts was scaled down to clinically realistic value of 2 million counts [15], to which Poisson noise was added. The noisy projection data were reconstructed using an iterative 3D order-subsets expectation-maximization (OS-EM) algorithm with 4 iterations and 8 subsets, as in typical SPECT reconstruction protocols. The OSEM technique compensated for attenuation and collimator-detector response. The reconstructed images were of dimensions $128 \times 128 \times 128$. The images were reconstructed at two voxel sizes, namely 2 mm and 4 mm. This was done to study the performance of the segmentation method for these two clinically relevant voxel sizes and evaluate the sensitivity of our method to voxel size. The overall process to generate the SPECT images is summarized in Fig. 2.2.

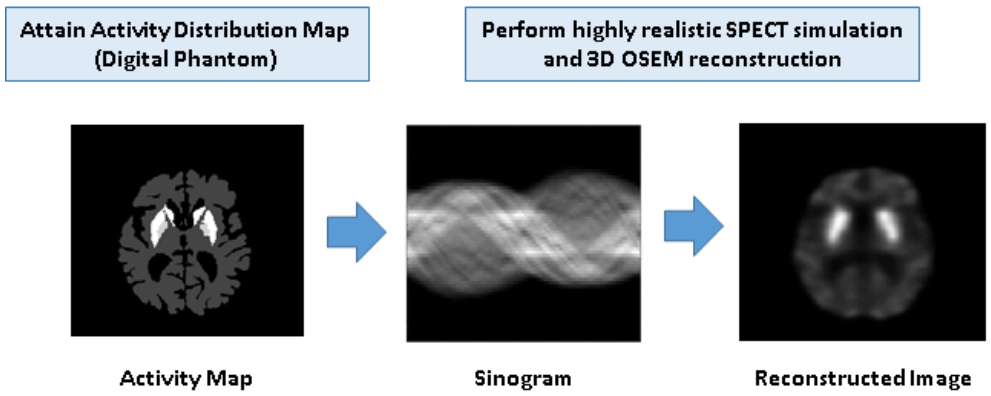

Figure 2.2: Workflow to simulate the SPECT images. DaT activity distribution map in relevant regions was attained from clinical data and structural boundaries from MR images. The digital phantom was then used for highly realistic SPECT simulation and 3D OS-EM reconstruction to generate reconstructed images.

Training and evaluation strategy

The 600 reconstructed 3D SPECT images were divided into two independent sets of 500 training images and 100 testing images. The training images were used to train the proposed method, while the testing images were used for qualitatively and quantitatively evaluating the performance of the method. The performance of the method was compared with several commonly used methods that have been used for SPECT segmentation. These included a Markov random fields-Gaussian mixture model (MRF-GMM)-based method [33, 38, 91], an active-contour-based technique, namely Snakes, [43], a thresholding-based technique, namely 40% SUV-max thresholding [46] and finally a state-of-the-art U-net-based technique [54] For the first three segmentation methods, the 40% SUV-max, Snakes and MRF-GMM, a manual input, which could be a seed voxel or an initial boundary estimate, was provided to the segmentation technique. The proposed method and the U-net-based method did not require any user inputs, and were fully automated.

Quantitative evaluation on the segmentation tasks was performed using metrics that evaluated spatial overlap and shape similarity. Note that the output from the segmentation method is an estimate of the fractional volume, which is a number between 0 and 1. Conventional segmentation methods typically assign a voxel to only a single class. For these methods, the spatial overlap is quantified using Dice similarity coefficient (DSC) and Jaccard similarity coefficient (JSC). Since our method yields a number between 0 and 1, we used the fuzzy analog of these metrics, namely the fuzzy DSC (fDSC) and fuzzy JSC (fJSC), as defined in Taha et al [95]. Higher values of these metrics indicate a more accurate segmentation. Also, the similarity in shapes between the true and estimated segmentations was quantified using the Hausdorff distance (HD) [31]. HD measures the maximum deviation between the predicted and true segmentation boundaries. Thus, lower value of HD represents higher shape similarity.

Studying effect of mismatch between MR and SPECT images

The proposed approach is trained in a setting where the alignment of the SPECT image with the corresponding MR images and the similarity of the MR anatomical and SPECT functional boundaries are enforced by default. However, a new SPECT image to which

this trained network is applied may not necessarily satisfy these conditions. For example, the new SPECT image may be misaligned compared to the MR images in the training set. Similarly, there may be a mismatch between the SPECT functional and the MR anatomical boundaries. To evaluate the sensitivity of our method to these sources of mismatch, we conducted the experiments as described in the next two sub sections.

Misalignment between MR and SPECT images: Our network was trained using a clinical MR population that was registered on the MNI space. In a realistic scenario, it may be possible that the SPECT scan of a new patient may be misaligned with this space. To simulate this effect, we evaluated the performance of our method when input SPECT test images were misaligned compared to the MR image population. A total of 100 test images were misaligned by rotating them in steps of 2 degrees, for up to a maximal rotation of $\pm 10^{\circ}$. The misalignment was introduced in the x-y plane. The sensitivity of the network to this misalignment was quantified using the fDSC metric.

Mismatch between functional SPECT and anatomical MR boundaries: The MR images provide the anatomical boundaries of the caudate, putamen, and GP regions. In contrast, the SPECT images provide the functional boundaries of these regions. In SPECT images of patients with higher severity of PD, the functional boundary of the putamen is typically smaller on the lower side of putamen in an axial view often asymmetrically [72]. As patients with PD progress, it has been observed that the affected putamen changes from a bean shape to a smaller size and circular shape in the SPECT image. In other words, it appears that the functional boundary of putamen is smaller. Further, uptake in the GP is typically non-existent in patients with more severe PD [52]. Thus, in summary, there is a potential of mismatch between the functional boundaries as defined on the SPECT and the anatomical boundaries as defined on the MR images. This is as shown in example in Fig. 2.5. We investigated the sensitivity of our method to this mismatch. For this purpose, in the test set, we simulated SPECT images with no uptake in the GP and progressively reduced functional size of the putamen, corresponding to different levels of disease severity. All 100 test subjects were used in this study. In each test subject, the functional boundary of the putamen was reduced compared to the anatomical boundary in steps of 10%, to up to 90%. In this study, only functional boundaries are affected and anatomical boundaries are not changed

2.3 Results

2.3.1 Qualitative evaluation

We first present representative qualitative results that provide context to the quantitative findings discussed in the next section. The segmentation boundaries estimated using the different methods for 2 mm voxel size SPECT images are shown in Fig. 3.1. The proposed method closely matched the ground-truth boundary. This is shown more clearly using the zoomed results in Fig. 2.4. These figures also illustrate the challenging nature of the segmentation task, as due to PVEs, the boundary between the different regions is highly blurred. As a result of this, the 40% SUV-max and active-contours method were not even able to segment the various regions separately. The MRF-GMM technique could segment three regions but the overlap between the predicted and the ground truth was not that high. In contrast, the proposed method yielded accurate segmentation of all the individual regions.

In Fig. 2.5, a visual comparison of performance of proposed segmentation method is provided for a healthy and a diseased patient. In the healthy patient, the anatomical and functional boundaries match. In the diseased patient, the functional boundary of the putamen is reduced and there is no uptake in the GP. The proposed segmentation method yielded a similar delineation as the true functional boundary in both these cases. Also, note that the proposed segmentation method did not yield a functional boundary for the GP region, thus correctly reflecting the zero-valued uptake in the GP and further demonstrating the accuracy of the proposed method.

2.3.2 Quantitative evaluation

In our qualitative results, we observed that the 40% SUV-max and Snakes methods were unable to separately segment caudate, putamen and GP regions. Thus, in the quantitative evaluations, the resultant total regions of striatal and pallidal region were used for 40% SUV-max and Snakes methods. In other words, since these methods provided a single combined segmentation of these regions, the combined regions were used for the quantitative studies. The top row in Fig. 2.6 shows that for the voxel size of 2 mm, the proposed method

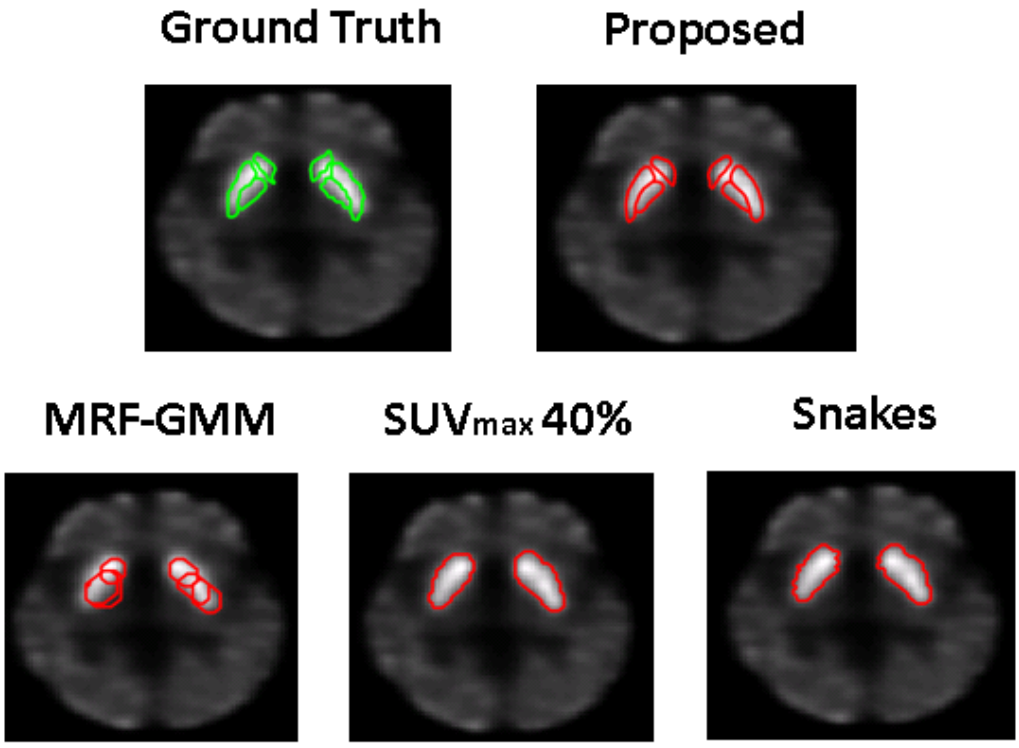

Figure 2.3: Visual comparison of the segmentation methods

outperformed other segmentation methods on the basis of the fDSC, fJSC, and HD metrics (p value <0.01). Also, the proposed method yielded a fDSC close to 0.8 for all the regions, thus indicating an accurate segmentation [105]. The existing semi-automated methods were highly inaccurate for the caudate and GP regions. While the proposed and the U-net-based methods were more accurate for these regions, the proposed method significantly outperformed the U-net-based method (p value <0.01).

Similar results were seen for the reconstructed images with voxel size of 4 mm on each side, as shown in the bottom row of Fig. 2.6. Further, the values of fDSC, fJSC and HD remained relatively unchanged in going from 2 mm voxel size to 4 mm voxel size for the proposed method. This indicates the relative insensitivity of the method to change in voxel sizes. In contrast, the performance of the U-net-based method, which does not model TFEs, significantly deteriorated for the higher voxel size. This was because the proposed method accounts for the TFEs unlike the U-net-based method.

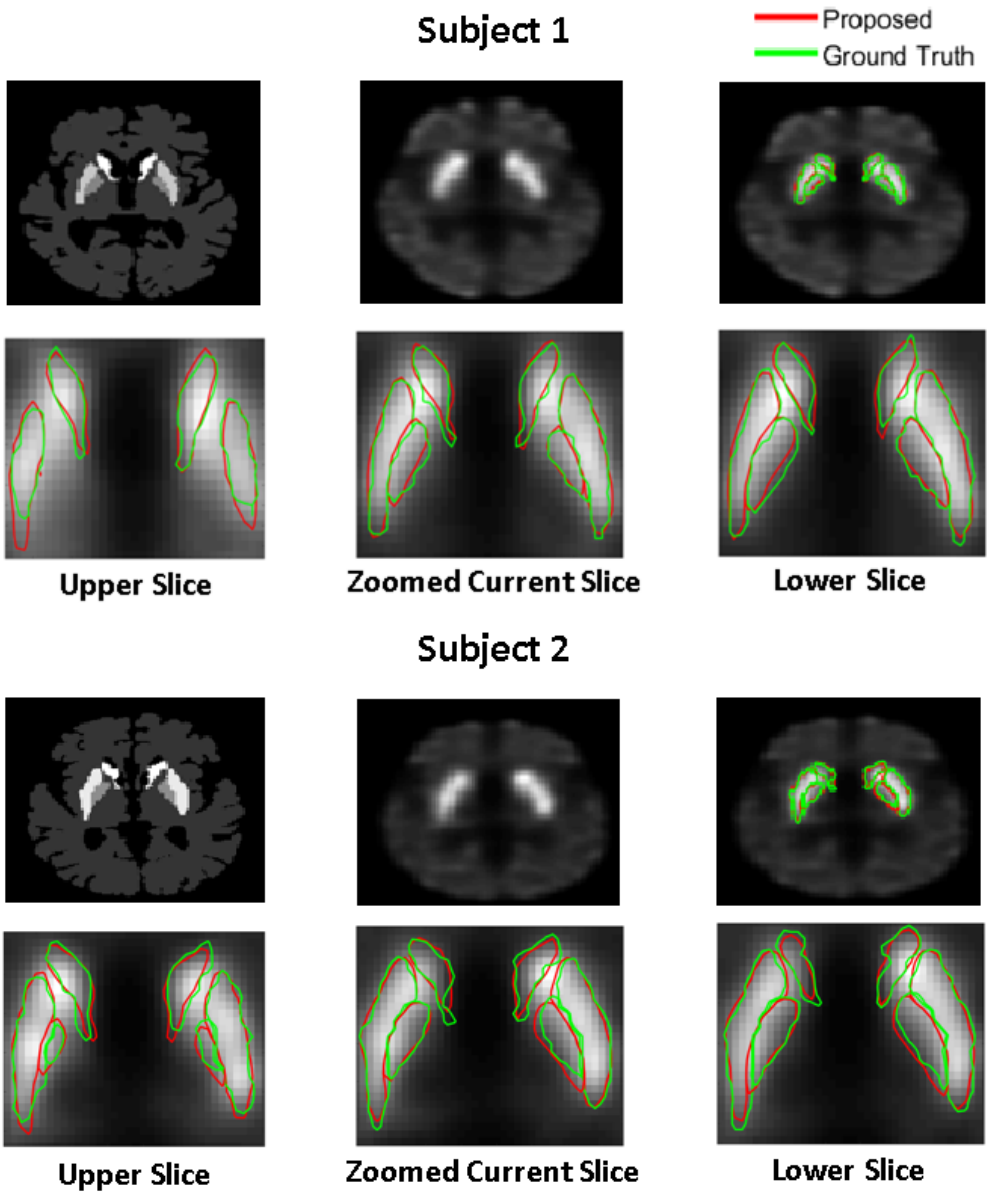

Figure 2.4: 3D segmentation of the proposed method and comparison with the ground truth. The upper slice shows an axially upper slice and lower slice shows axially lower slice of the current slice.

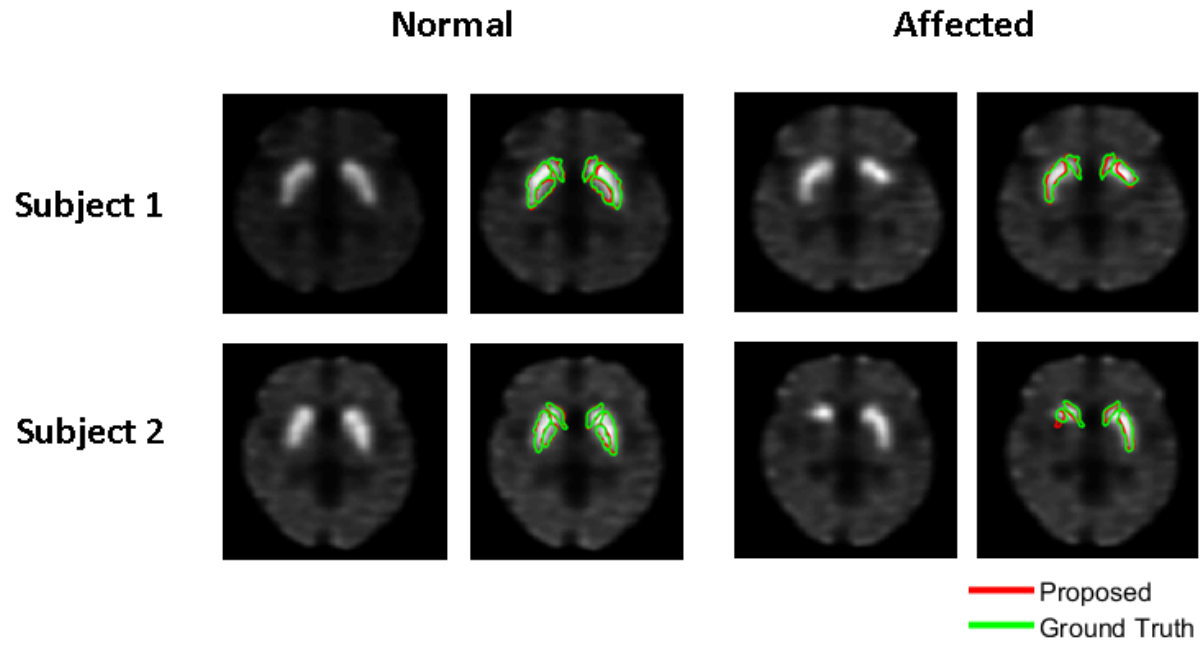

Figure 2.5: 3D segmentation of the proposed method for visual comparison of normal activity and affected DaT levels where a asymmetrically reduced activity in the putamen is simulated.

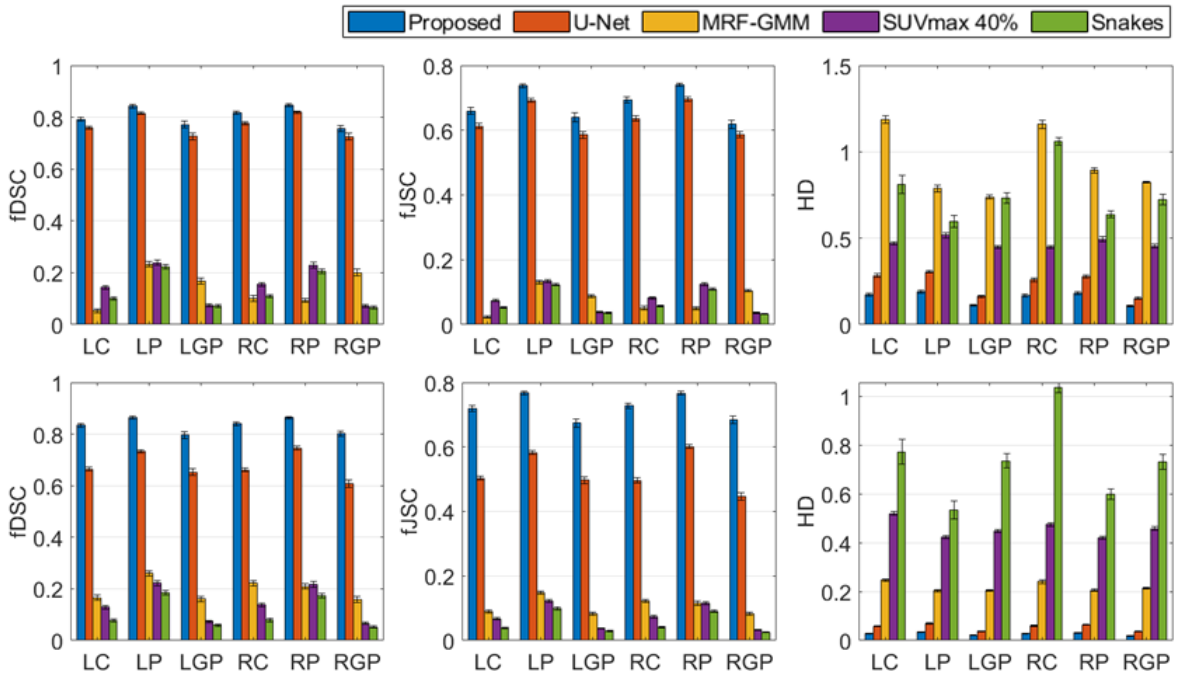

Figure 2.6: Comparison of the fDSC, fJSC, and HD from left to right respectively obtained using the five segmentation methods that allows separate segmentation for images with 2 mm voxel size (top row) and 4 mm voxel size (bottom row).

The accuracy of the proposed method when the MR and SPECT images were misaligned is shown in Fig. 3.2. The proposed method continued to yield accurate segmentation between -4 and 4 degree of misalignment. Also, for larger misalignment, while the performance of the proposed method was slightly affected, the fDSC values were still close to 0.8 for both 2 mm and 4 mm voxel sizes, indicating a good segmentation accuracy.

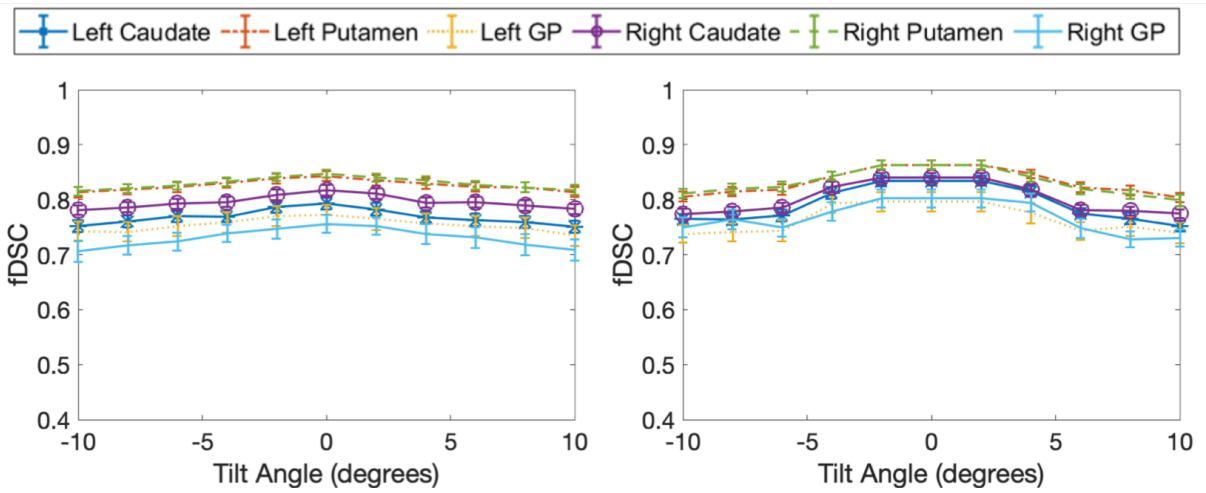

Figure 2.7: The accuracy when MR and SPECT images are mis-registered. The left figure shows results with 2 mm voxel size and right figure shows results with 4 mm voxel size.

The sensitivity of the method to mismatch between the functional boundary and the MR-defined anatomical boundary is shown in Fig. 2.8. As the available functional boundary decreased, the fDSC scores reduced. However, the proposed method yielded more than 0.7 DSC value for up to the case where the functional boundary of the putamen was 40% of the anatomical boundary.

2.4 Discussions

Overall, the results demonstrate the efficacy of the proposed method in reliably segmenting the caudate, putamen, and GP regions from DaT-scan SPECT images. The ability of segmenting the small-sized GP region in particular, is distinctive as the GP is visually almost impossible to demarcate on the SPECT images. It is well known that the GP plays an important role in the movement-related direct and indirect pathways of basal ganglia

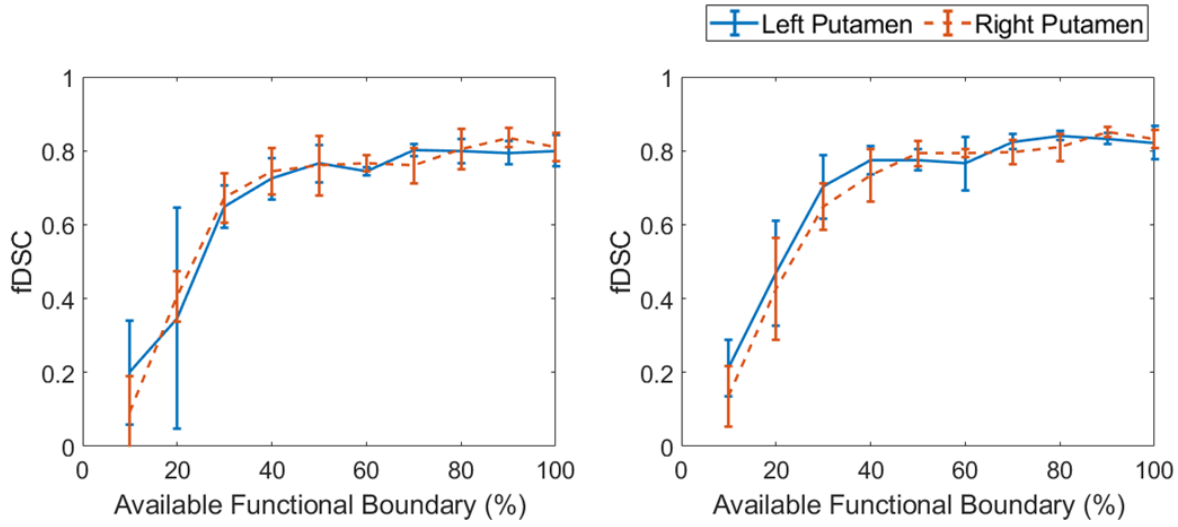

Figure 2.8: The figure shows results with 2 mm voxel size on the left and 4 mm voxel size on the right with asymmetrically reduced functional uptake in the left and right putamen.

[49]. There has been interest in studying the plasticity of the nigro-pallidal pathway [100]. Quantification of the DaT uptake in the pallidal regions may provide new insights on this plasticity. Several post-mortem studies have shown evidence of DaT uptake in the pallidal regions [8, 75] DaT-scan SPECT studies provide a mechanism to study these effects *in vivo* but this has been hindered by the lack of tools to segment the pallidal regions on the SPECT images. Our results show that the proposed method can help to address this challenge. Thus, this result opens up a new and important research frontier on analysing the functional characteristics of the GP region in patients with Parkinson's disease. Additionally, the method also provides an accurate delineation of the caudate and putamen regions in the SPECT images. This provides tools to conduct shape analysis of these regions, which may lead to new biomarkers for diagnosis and measuring severity of Parkinson's disease.

We observe from Fig. 2.6 that the proposed method outperforms several existing segmentation methods, including a U-net-based approach [54]. The U-net based approach also learns anatomical variability and PVEs arising due to limited system resolution, but does not account for the TFEs, unlike the proposed method. An increase in the voxel size in SPECT increases the TFEs. Thus, the proposed method performs better than other segmentation methods especially when the voxel size is larger. This explains the larger difference in the DSC and JSC values between the proposed and the U-net-based method when the reconstructed images have 4 mm voxel size. The higher accuracy of the proposed method at 4 mm

voxel size is especially significant as many clinical DaT SPECT scans are recommended and conducted with 4 mm voxel sizes [15]. Next, we also observe in Fig. 2.6 that an increase in the voxel size from 2 mm to 4 mm did not affect the DSC of the proposed method, but the DSC of the U-net-based approach decreased by more than 10%. This provides evidence that the proposed approach is relatively robust to changes in voxel size. This again demonstrates that accounting for TFEs provides distinct and clinically relevant advantages to this method compared to existing methods.

Another class of methods to segment the striatal regions in DaTscan SPECT images have been those that use the MR images acquired from a different scanner [77]. These methods have not been evaluated on the task of segmenting GP. Further, these methods require that both SPECT and MR images of the same patient be available, which is typically not the case, and even when available, is likely from a different time point. While there has been some recent progress in the area of developing simultaneous SPECT/MR systems [32], no clinical simultaneous SPECT/MRI systems are currently available. In contrast, the proposed method does not require the corresponding MR image from the patient to perform the segmentation and works on stand-alone SPECT images.

We also observe that the proposed method is accurate even when there is some degree of mismatch between the SPECT and MR images. While this observation may seem confounding at first, note that the proposed method estimates the posterior mean of the fractional volumes that a region occupies within a voxel. This posterior mean depends on the input test SPECT image that is being segmented. Thus, the performance of the method is not necessarily effected when the mismatch between the training and test set is small. Developing a theoretical formalism that can quantify the tolerability of this mismatch is an important research frontier. Nevertheless, our results in Fig. 3.2 show that for up to 10% of misalignment between SPECT and MR images, the performance of the method is relatively robust. This is encouraging as the main challenge occurs when the degree of misalignment is small, since that is visually difficult to identify. In contrast, higher degrees of misalignment are visually easier to identify, and thus, in those cases, the SPECT images can be first registered to the MR MNI space. After registration, there may still be small degrees of misalignment, but our results show that this would not affect the performance of the method. Similarly, our results in Fig. 2.8 show that the method yields accurate segmentation even when the functional boundary is only 40 % of the anatomical boundary. Clinically, functional boundaries

lower than these are typically not observed [71]. Thus, this result provides evidence that the proposed method is relatively robust to mismatches between the functional and anatomical boundaries for clinically relevant purposes.

Our study has some limitations. The first limitation is that the method was evaluated using simulation studies. While the simulations used clinical MR images as anatomical templates, were clinically guided and highly realistic, they may have not been able to account for all sources of population variability and account for all aspects of the imaging physics. Evaluation using physical-phantom and patient-data-based studies can help address this limitation. Evaluation using physical phantoms will model all aspects of the system instrumentation. Similarly, evaluation with clinical datasets will account for any missed sources of population variability. This is an important area of future study. Another limitation is that in this manuscript, we focused on the task of segmenting the caudate, putamen and GP regions in the DaT-scan images and considered the rest of the region as background. However, post-mortem studies indicate DaT uptake in other regions in the basal ganglia such as the nucleus accumbens and substantia nigra [93]. Also, the GP can itself be separate into two parts, namely the internal and the external GP. Results from this study motivate extending the proposed approach to consider these segmentation tasks. Finally, in our simulation studies, we assume that the uptake within the various regions is uniform. However, the tracer uptake within the putamen may be heterogeneous in patients with PD. Modeling this heterogeneity and evaluating the performance of the proposed segmentation method in the presence of this heterogeneity are important research areas.

2.5 Conclusions

An estimation-based fully automated method to segment the caudate, putamen, and globus pallidus regions from 3D DaT-scan SPECT images has been proposed. The method accounts for both sources of partial-volume effects in SPECT images, namely system-generated blur and tissue-fraction effects. Essentially, the method estimates the posterior mean of the fractional volume that the different regions occupy in each voxel, a distribution of which can be obtained from existing MR image populations. Rigorous evaluation using realistic simulation studies conducted with clinically derived data demonstrated that the method

provided accurate delineation of the caudate, putamen and GP for 3D DaTscan SPECT images. The method outperformed existing methods including a U-net-based approach, and was relatively insensitive to the choice of two different voxel sizes. Further, the method was robust to misalignments between the SPECT test image and MR image populations, and mismatches between the MR anatomical boundary and the functional boundary in the SPECT test image. Overall, the results provide strong evidence of the efficacy of the segmentation method and motivate further evaluation with physical phantoms and patient data.

Chapter 3

Compensating for partial volume effects in DaTscan SPECT

3.1 Introduction

A major challenge to quantitative DaTscan imaging is the partial volume effects that are present in DaTscan SPECT images. Due to limited collimator-detector response of the system, structures smaller than 3 times of FWHM are more prone to PVEs [103, 17]. The issue is compounded when these small regions are adjacent to each other, as is the case with DaTscan SPECT where the caudate, putamen, and globus pallidus (GP) are often lying next to each other [103, 17]. Also, tissue fraction effects (TFEs) due to generally larger voxel sizes in SPECT add to the PVEs. These limitations often lead to large bias in brain SPECT when performing quantitative studies [103, 18, 17]. In previous SPECT simulations and quantification of regions, there has been a reported underestimation of uptake within region of interest that was especially significant as the size of structures decreased [103]. This occurred because of PVEs related to the spatial resolution of the imaging system [103].

To compensate for these effects, a partial volume compensation method has been previously introduced by Rousset et al [81]. The method used a geometric transfer matrix (GTM) to calculate the spill over effects of an ROI and surrounding regions and incorporated these effects for correction of mean uptake value [81]. In previous studies, application of this method led to significantly lower biases. [18, 17]. In these studies, acquiring a ground-truth mask for the region of interest (ROI) was needed. However, in clinical settings, ground-truth ROIs and accurate segmentation of ROIs may not be available. The segmentation method

proposed in Chapter 2 provides a mechanism to address this issue. We now propose a novel PVC technique that builds upon the segmentation technique proposed in Chapter 2.

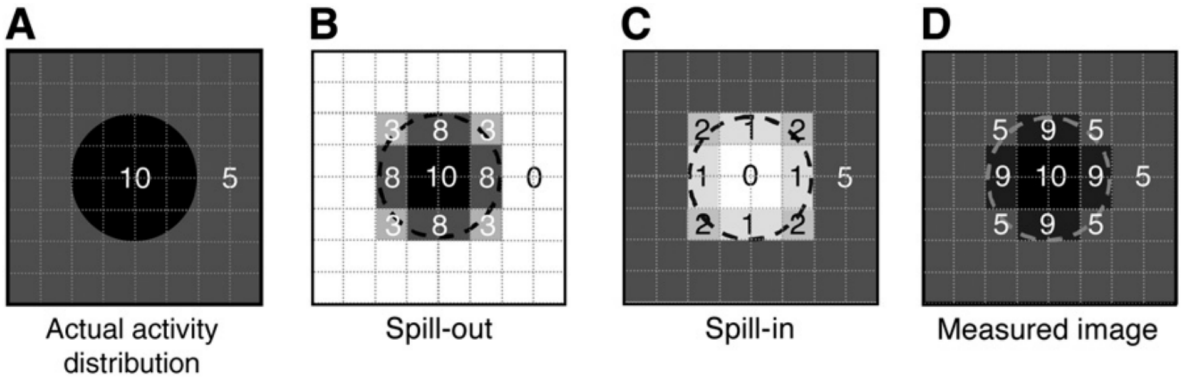

Figure 3.1: (A) Original true activity distribution. (B) The spilling out effect. (C) Spilling in effect due to spilling out from (B). (D) Resulted measured image. Original figure from Soret et al. [87]

3.2 Methods

3.2.1 Theory for Continuous GTM Method

Let $f(\mathbf{r})$ denote the true tracer activity distribution over K number of distinct tissue components each with a ROI denoted by $\chi_i(\mathbf{r})$.

$$f(\mathbf{r}) = \sum_{i=1}^{K} \lambda_i \chi_i(\mathbf{r}). \tag{3.1}$$

Consider imaging this tracer distribution through a SPECT system with field of view of $\mathcal{S}_f$. The SPECT imaging process can be described as a linear operator. Also SPECT reconstruction methods that sufficiently compensate for image-degrading processes can be described as approximately linear [34]. Here we assume that the SPECT system and the reconstruction operator can be together described as a linear operator. Let $h_m(\mathbf{r})$ denote the M-dimensional kernel of this linear operator. Let $\hat{\theta}_m$ is the reconstructed SPECT image

resulted from tracer distribution $f(\mathbf{r})$.

$$\hat{\theta}_m = \int_{\mathcal{S}_f} \mathrm{d}^3\mathbf{r} h_m(\mathbf{r}) f(\mathbf{r}). \tag{3.2}$$

Let r' denote the 3D spatial coordinate in the reconstructed image space. The reconstructed image $\hat{f}(\mathbf{r}')$ is represented in discrete space with the voxel expansion function given by $\phi_m(\mathbf{r}')$ and combined with Eq. 3.2 to represent reconstructed image continuous space.

$$\hat{f}(\mathbf{r}') = \sum_{m=1}^{M} \hat{\theta}_m \phi_m(\mathbf{r}') \tag{3.3}$$

$$= \int_{\mathcal{S}_f} \mathrm{d}^3\mathbf{r} \sum_{m=1}^{M} h_m(\mathbf{r}) \phi_m(\mathbf{r}') f(\mathbf{r}) \tag{3.4}$$

$$= \int_{\mathcal{S}_f} \mathrm{d}^3\mathbf{r} k(\mathbf{r}', \mathbf{r}) f(\mathbf{r}). \tag{3.5}$$

where,

$$k(\mathbf{r}', \mathbf{r}) = \sum_{m=1}^{M} h_m(\mathbf{r}) \phi_m(\mathbf{r}'). \tag{3.6}$$

Substituting Eq. 3.1 into Eq. 3.5, yields

$$\hat{f}(\mathbf{r}') = \sum_{i=1}^{K} \lambda_i \int_{\mathcal{S}_f} \mathrm{d}^3\mathbf{r} k(\mathbf{r}', \mathbf{r}) \chi_i(\mathbf{r}). \tag{3.7}$$

Denote the volume and mean estimated activity uptake in the j^{th} ROI by V_j and $\lambda_j^{'}$. Then,

$$\lambda_j' = \frac{1}{V_j} \int_{\mathcal{S}_f} \mathrm{d}^3\mathbf{r}' \hat{f}(\mathbf{r}') \chi_j(\mathbf{r}) \tag{3.8}$$

$$= \frac{1}{V_j} \sum_{n=1}^{N} \lambda_i \int_{\mathcal{S}_f} \mathrm{d}^3\mathbf{r}' \chi_j(\mathbf{r}') \int_{\mathcal{S}_f} \mathrm{d}^3\mathbf{r} k(\mathbf{r}', \mathbf{r}) \chi_i(\mathbf{r}). \tag{3.9}$$

where in the second step, we substitute the expression from Eq. 3.7. For simplicity of notation, we define the weight coefficients w_{ji}.

$$\lambda'_j = \sum_{n=1}^{N} \lambda_i w_{ji}. \tag{3.10}$$

where from Eq. 3.9, w_{ji} is defined

$$w_{ji} = \frac{1}{V_j} \int_{\mathcal{S}_f} \mathrm{d}^3\mathbf{r}' \chi_j(\mathbf{r}') \int_{\mathcal{S}_f} \mathrm{d}^3\mathbf{r} k(\mathbf{r}', \mathbf{r}) \chi_i(\mathbf{r}) \tag{3.11}$$

$$= \frac{1}{V_j} \int_{\mathcal{S}_f} \mathrm{d}^3\mathbf{r}' \chi_j(\mathbf{r}') \int_{\mathcal{S}_f} \mathrm{d}^3\mathbf{r} \sum_{m=1}^{M} h_m(\mathbf{r}) \phi_m(\mathbf{r}') \chi_i(\mathbf{r}). \tag{3.12}$$

For simplicity, we define w_{ji} in operator notation. Denote the SPECT projection and reconstruction operators by $\mathcal{P}$ and $\mathcal{R}$. Let $\mathcal{D}^\dagger$ represents the adjoint of the discretization operator. This adjoint operator is given by

$$[\mathcal{D}^\dagger \hat{\theta}] = \sum_{m=1}^{M} \hat{\theta}_m \phi_m(\mathbf{r}). \tag{3.13}$$

Then, w_{ji} is given by

$$w_{ji} = \frac{1}{V_j} ROI_j \cdot \mathcal{D}^\dagger\{\mathcal{R}\{\mathcal{P}\{ROI_i\}\}\}. \tag{3.14}$$

With this definition for the weight coefficient, using Eq. 3.10, the activity uptake in the j^{th} ROI from the reconstructed image can be written in matrix form as follows:

$$\begin{bmatrix} \lambda'_1 \\ \lambda'_2 \\ \vdots \\ \lambda'_N \end{bmatrix} = \begin{bmatrix} \omega_{11} & \omega_{21} & \cdots & \omega_{N1} \\ \omega_{12} & \omega_{22} & \cdots & \omega_{N2} \\ \vdots & \vdots & \ddots & \vdots \\ \omega_{1N} & \omega_{2N} & \cdots & \omega_{NN} \end{bmatrix} \begin{bmatrix} \lambda_1 \\ \lambda_2 \\ \vdots \\ \lambda_N \end{bmatrix}$$

Denote the vectors $[\lambda_1 \dots \lambda_N]$ and $[\lambda'_1 \dots \lambda'_N]$ by Λ and Λ', respectively. Also, denote the matrix consisting of the weights by W. Then, the above equation can be written in vector notation as follows:

$$\Lambda' = W\lambda. \tag{3.15}$$

Therefore, to estimate λ, we can simply taken the inverse of the W matrix. In other words

$$\Lambda = W^{-1}\Lambda'. \tag{3.16}$$

3.2.2 Evaluation of the Proposed Method

To quantitative evaluate the proposed PVC method, we first used the segmentation method proposed in Chapter 2 to calculate the average mean uptake of caudate, putamen and globus pallidus regions from the reconstructed images for both hemispheres. However, the proposed segmentation did not include segmentation of the background region of the brain. Thus, the segmentation of the background wass estimated by subtracting regions of caudate, putamen and globus pallidus from a normalized reconstructed image. This allowed a fair estimation of the background with only using already available reconstructed images and segmentations from the proposed method.

The segmented masks of regions are projected and reconstructed using the same simulation and reconstruction protocol that are used for DaTScan images. Then by using the reconstructed images of the segmented regions and continuous GTM method, corrected mean uptakes of the regions are calculated for both 2 mm and 4 mm voxel sizes. The experiment was performed for the 100 test subjects described in Chapter 2.

3.3 Results

As shown in Table 3.1, the percent bias of caudate improved from $\sim 47\%$ to ~ 34 %, that of putamen improved from ~ 27 % to ~ 15 % for 2 mm voxel size. The percent bias of globus pallidus and background also improved, but the improvement wasn't significant. Also, the PVC results for voxel size of 4 mm is shown in Table 3.2. The percent bias of caudate improved significantly from $\sim 44\%$ to ~ 11 %, that of putamen improved from ~ 23 % to ~ 12 %. Similarly to results of 2 mm voxel size, the correction didn't have significant effect on the percent bias of globus pallidus and the background. Generally, the uncorrected percent bias for 2 mm voxel size was marginally larger than that of 4 mm voxel size DaTScan images.

	Uncorrected Bias (%)	Corrected Bias (%)
Left Caudate	46.7419	31.7106
	45.4816 48.0022	30.2190 33.2022
Left Putamen	26.1385	13.9927
	24.6306 27.6465	12.0097 15.9756
Left Globus Pallidus	23.6298	22.5707
	20.6010 26.6587	19.4549 25.6866
Right Caudate	48.0064	36.664
	46.6916 49.3212	35.2706 38.0573
Right Putamen	28.0093	16.503
	26.5426 29.4761	14.6159 18.3900
Right Globus Pallidus	23.7889	22.6295
	20.7527 26.8251	19.4832 25.7757
Background	43.0431	40.3054
	37.4962 48.5900	34.4820 46.1289

Table 3.1: The uncorrected bias and corrected bias in percentage of mean uptake values for both left and right caudate, putamen, globus pallidus and the background for DaTScan images with 2 mm voxel size are shown

3.4 Discussions and Conclusion

The improved segmentation results from Chapter 2 has a lot of potential for direct analysis of the segmented regions of the caudate, putamen and globus pallidus.

	Uncorrected Bias (%)	Corrected Bias (%)
Left Caudate	43.6016	10.5099
	42.6330 44.5702	9.2155 11.8043
Left Putamen	22.2876	12.824
	20.7849 23.7902	11.2412 14.4067
Left Globus Pallidus	22.7521	21.8267
	20.3022 25.2019	19.0842 24.5692
Right Caudate	44.2827	12.4345
	43.2589 45.3065	11.0338 13.8353
Right Putamen	23.843	12.0203
	22.3781 25.3079	10.4671 13.5735
Right Globus Pallidus	23.6498	24.2659
	21.0415 26.2580	21.4030 27.1288
Background	51.7421	50.898
	47.0170 56.4673	46.0639 55.7322

Table 3.2: The uncorrected bias and corrected bias in percentage of mean uptake values for both left and right caudate, putamen, globus pallidus and the background for DaTScan images with 4 mm voxel size are shown

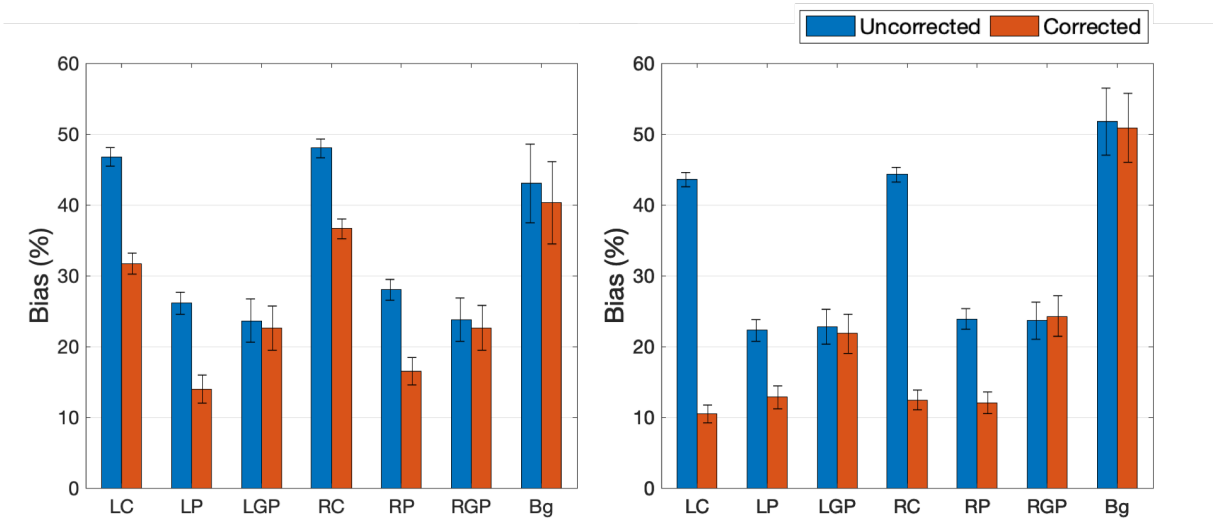

Figure 3.2: Plot for the percent bias comparison between corrected and uncorrected results for 2 mm voxel size on the left and 4 mm voxel size on the right

The quantification results of caudate and putamen improved significantly with PVC method using GTM based on proposed segmentation as shown in Table 3.1 and Table 3.2. The PVC results for 4 mm voxel size improved more significantly than those of 2 mm voxel size

similarly with the segmentation results in Chapter 2. This improvement is clinically relevant as most clinical DaTScan protocols are conducted to create $\sim$ 4 mm pixel size images [15]. However, the results with globus pallidus and the background didn't improve as significantly. This motivates the need for even more improved PVC methods. An interesting direction is extending a perturbation-based GTM (pGTM) approach as proposed in Du et al. [17] . The pGTM approach has been observed to yield improved performance on PVC by attempting to account for the non-linearity of the reconstruction operator. Extending this approach for a continuous estimate of the region boundary can further improve quantification performance and is an important research frontier.

In summary, the proposed PVC method integrated with the segmentation method shows significant potential for improving estimates of uptake within regions of interest from the DaTscan SPECT images, that it does not need the ground truth boundaries of the region of interest as needed in previous studies [17, 87, 81]. Also, the method is fully automated as it does not require any manual segmentation of the different regions in the SPECT image.

Chapter 4

Conclusions and Future work

4.1 Overview

This study has been conducted in order to address in an important need for developing biomarkers to improve diagnosis and measure the severity of PD. The key goal was to achieve reliable quantification of uptake from the DaTscan SPECT images. Reliable quantification from reconstructed images requires an accurate segmentation of these regions. This was a challenge for DaTScans due to the limited spatial resolution, partial volume effects, high noise, physiological variability and small size of the regions of interest. To address these issues, we developed a 3D physics-guided estimation-based method by integrating the prior distribution acquired from MR images for DaTScan SPECT image segmentation. A Bayesian approach that estimates the posterior-mean of the fraction volume that a particular regions of interest occupy within each voxel of a SPECT image was developed. The method was implemented using an auto-encoder that was optimized and trained with 500 images and tested on 100 images. The method yielded quantitatively and qualitatively improved segmentation results outperformed previously developed methods, and was relatively insensitive to different types of mismatch between the training and testing. Following this, a geometric transfer matrix (GTM)-based approach was extended to perform partial volume compensation (PVC) from the DaTscan SPECT images. A GTM method for partial volume compensation used the segmented masks estimated from the proposed segmentation method and provided significantly improved estimate of average uptake in the striatum region.

4.2 Evaluation with Physical-Phantom Study

As mentioned in Chapter 2, an important research frontier is validating the segmentation method using physical-phantom studies. For this purpose, we have collaborated with 3D printing lab at Mallinckrodt Institute of Radiology for designing and printing 3D physical brain phantom that has separate tracer fillable regions for caudate, putamen, globus pallidus and the background as shown in Fig 4.1 [64]. The physical phantom experiment, where we would fill different regions with different Ioflupane uptake values and scan with a SPECT system available at Washington University School of Medicine, could help validate the proposed method.

Figure 4.1: Printed brain phantom

4.3 Evaluation with Patient Studies

It is important to perform a patient study for final validation of the proposed method if clinical data is available. This would require obtaining at large number of clinical DaTScan images. There is an open database from Parkinson's progression marker initiative (PPMI) where hundreds of DaTScan images are available. This database provides a resource to evaluate the proposed methods.

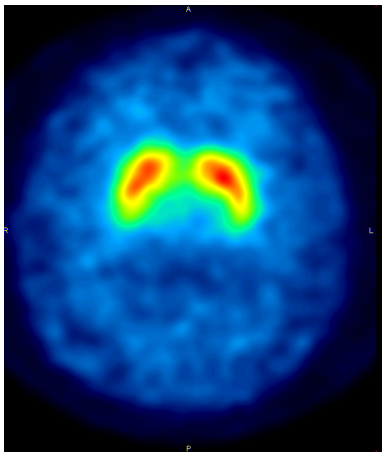

Figure 4.2: Axial DaTScan image from PPMI. Image adopted from PPMI website [64]

4.4 Performing Quantification with List-mode Data

Another challenge in evaluation with patient data is the lack of ground-truth quantitative values. This lack of ground-truth data is generally an issue in evaluating quantitative imaging methods. To address this issue, no-gold-standard (NGS) evaluation techniques have been developed [36, 39, 34, 37, 35, 47, 27]. In this thesis, we explored the use of existing NGS evaluation procedures for evaluating the DaTscan SPECT image analysis methods. However, the performance of these methods was limited. More recently, a novel NGS evaluation procedure has been developed [56] that addresses some of the limitations of the existing NGS evaluation techniques. Developing and evaluating this NGS evaluation procedure for quantitatively evaluating the proposed segmentation method with patient data is another important research direction.

4.5 Shape and Texture Analysis

As shown in Chapter 2, significantly improved segmentation accuracy of caudate, putamen and globus pallidus has potential for several practical implications. First, because previous shape and texture analysis methods of DaTScan images were conducted using simple and less reliable segmentation methods such as thresholding, the improved segmentation accuracy of the proposed method could help and improve predicted outcome of these studies [89, 76].

Also, separate segmentation of caudate, putamen and globus pallidus could lead to separate shape analysis of different regions of the brain which could be more advantageous that evaluating the striatum as a whole. Further, significantly improved percent bias of mean uptake for caudate and putamen have potential for future usage and further validation.

References

[1] Andrew L Alexander, Jee Eun Lee, Mariana Lazar, and Aaron S Field. Diffusion tensor imaging of the brain. *Neurotherapeutics*, 4(3):316–329, 2007.

[2] Toshiyuki Aoi, Tsutomu Zeniya, Hiroshi Watabe, Hossain M Deloar, Tetsuya Matsuda, and Hidehiro Iida. System design and development of a pinhole SPECT system for quantitative functional imaging of small animals. *Annals of nuclear medicine*, 20(3):245–251, 2006.

[3] Antonio Augimeri, Andrea Cherubini, Giuseppe Lucio Cascini, Domenico Galea, Maria Eugenia Caligiuri, Gaetano Barbagallo, Gennarina Arabia, and Aldo Quattrone. CADA—computer-aided DaTSCAN analysis. *European journal of nuclear medicine and molecular imaging physics*, 3(1):4, 2016.

[4] Kosmas Badiavas, Elisavet Molyvda, Ioannis Iakovou, Magdalini Tsolaki, Kyriakos Psarrakos, and Nikolaos Karatzas. SPECT imaging evaluation in movement disorders: far beyond visual assessment. *European journal of nuclear medicine and molecular imaging physics*, 38(4):764–773, 2011.

[5] TC Booth, M Nathan, AD Waldman, A-M Quigley, AH Schapira, and J Buscombe. The role of functional dopamine-transporter SPECT imaging in Parkinsonian syndromes, part 1. *American Journal of Neuroradiology*, 36(2):229–235, 2015.

[6] K Ray Chaudhuri and Anthony HV Schapira. Non-motor symptoms of Parkinson's disease: dopaminergic pathophysiology and treatment. *The Lancet Neurology*, 8(5):464–474, 2009.

[7] Junyu Chen, Abhinav K Jha, and Eric C Frey. Incorporating CT prior information in the robust fuzzy C-means algorithm for QSPECT image segmentation. In *Medical Imaging 2019: Image Processing*, volume 10949, page 109491W. International Society for Optics and Photonics, 2019.

[8] Brian J Ciliax, Genny W Drash, Julie K Staley, Sharon Haber, Catherine J Mobley, Gary W Miller, Elliott J Mufson, Deborah C Mash, and Allan I Levey. Immunocytochemical localization of the dopamine transporter in human brain. *Journal of Comparative Neurology*, 409(1):38–56, 1999.

[9] Brian J Ciliax, Craig Heilman, Lidia L Demchyshyn, Zdenek B Pristupa, Ernest Ince, Steven M Hersch, Hyman B Niznik, and Allan I Levey. The dopamine transporter: immunochemical characterization and localization in brain. *Journal of Neuroscience*, 15(3):1714–1723, 1995.

[10] National Research Council et al. Single Photon Emission Computed Tomography. In *Mathematics and Physics of Emerging Biomedical Imaging*. National Academies Press (US), 1996.

[11] Antonia Creswell, Kai Arulkumaran, and Anil A Bharath. On denoising autoencoders trained to minimise binary cross-entropy. *arXiv preprint arXiv:1708.08487*, 2017.

[12] Jeffrey L Cummings, Michael J Fine, Igor D Grachev, C Rick Jarecke, Meridith K Johnson, Phillip H Kuo, Kenneth L Schaecher, JA Oberdorf, M Rezak, DE Riley, et al. *Effective and Efficient Diagnosis of Parkinsonism: The Role of Dopamine Transporter SPECT Imaging with Ioflupane I-123 Injection (DaTscan TM)*. Managed Care & Healthcare Communications, 2014.

[13] E Gordon DePuey. Advances in SPECT camera software and hardware: currently available and new on the horizon. *Journal of nuclear cardiology*, 19(3):551–581, 2012.

[14] Yuni K Dewaraja, Michael Ljungberg, and Kenneth F Koral. Monte Carlo evaluation of object shape effects in iodine-131 SPECT tumor activity quantification. *European journal of nuclear medicine*, 28(7):900–906, 2001.

[15] David SW Djang, Marcel JR Janssen, Nicolaas Bohnen, Jan Booij, Theodore A Henderson, Karl Herholz, Satoshi Minoshima, Christopher C Rowe, Osama Sabri, John Seibyl, et al. SNM practice guideline for dopamine transporter imaging with 123I-Ioflupane SPECT 1.0. *Journal of Nuclear Medicine*, 53(1):154–163, 2012.

[16] E Ray Dorsey, Robert G Holloway, and Bernard M Ravina. Biomarkers in Parkinson's disease. *Expert review of neurotherapeutics*, 6(6):823–831, 2006.

[17] Yong Du, Benjamin MW Tsui, and Eric C Frey. Partial volume effect compensation for quantitative brain SPECT imaging. *IEEE transactions on medical imaging*, 24(8):969–976, 2005.

[18] Georges El Fakhri, Stephen C Moore, Philippe Maksud, André Aurengo, and Marie Foley Kijewski. Absolute activity quantitation in simultaneous 123I/99mTc brain SPECT. *Journal of Nuclear Medicine*, 42(2):300–308, 2001.

[19] Stanley Fahn and David Sulzer. Neurodegeneration and neuroprotection in Parkinson disease. *NeuroRx*, 1(1):139–154, 2004.

[20] Bruce Fischl. FreeSurfer. *Neuroimage*, 62(2):774–781, 2012.

[21] Brent Foster, Ulas Bagci, Awais Mansoor, Ziyue Xu, and Daniel J Mollura. A review on segmentation of positron emission tomography images. *Computers in biology and medicine*, 50:76–96, 2014.

[22] Curt R Freed, Paul E Greene, Robert E Breeze, Wei-Yann Tsai, William DuMouchel, Richard Kao, Sandra Dillon, Howard Winfield, Sharon Culver, John Q Trojanowski, et al. Transplantation of embryonic dopamine neurons for severe Parkinson's disease. *New England Journal of Medicine*, 344(10):710–719, 2001.

[23] Christopher G Goetz, Barbara C Tilley, Stephanie R Shaftman, Glenn T Stebbins, Stanley Fahn, Pablo Martinez-Martin, Werner Poewe, Cristina Sampaio, Matthew B Stern, Richard Dodel, et al. Movement Disorder Society-sponsored revision of the Unified Parkinson's Disease Rating Scale (MDS-UPDRS): scale presentation and clinimetric testing results. *Movement disorders: official journal of the Movement Disorder Society*, 23(15):2129–2170, 2008.

[24] Parkinson Study Group. Levodopa and the progression of Parkinson's disease. *New England Journal of Medicine*, 351(24):2498–2508, 2004.

[25] Rick C Helmich, Mark Hallett, Günther Deuschl, Ivan Toni, and Bastiaan R Bloem. Cerebral causes and consequences of Parkinsonian resting tremor: a tale of two circuits? *Brain*, 135(11):3206–3226, 2012.

[26] Rick C Helmich, Marcel JR Janssen, Wim JG Oyen, Bastiaan R Bloem, and Ivan Toni. Pallidal dysfunction drives a cerebellothalamic circuit into Parkinson tremor. *Annals of neurology*, 69(2):269–281, 2011.

[27] John W Hoppin, Matthew A Kupinski, George A Kastis, Eric Clarkson, and Harrison H Barrett. Objective comparison of quantitative imaging modalities without the use of a gold standard. *IEEE transactions on medical imaging*, 21(5):441–449, 2002.

[28] H Malcolm Hudson and Richard S Larkin. Accelerated image reconstruction using ordered subsets of projection data. *IEEE transactions on medical imaging*, 13(4):601–609, 1994.

[29] Andrew J Hughes, Susan E Daniel, Linda Kilford, and Andrew J Lees. Accuracy of clinical diagnosis of idiopathic Parkinson's disease: a clinico-pathological study of 100 cases. *Journal of Neurology, Neurosurgery & Psychiatry*, 55(3):181–184, 1992.

[30] Chauncey J Hunker and James H Abbs. Uniform frequency of Parkinsonian resting tremor in the lips, jaw, tongue, and index finger. *Movement disorders: official journal of the Movement Disorder Society*, 5(1):71–77, 1990.

[31] Daniel P Huttenlocher, Gregory A Klanderman, and William J Rucklidge. Comparing images using the Hausdorff distance. *IEEE Transactions on pattern analysis and machine intelligence*, 15(9):850–863, 1993.

[32] Brian F Hutton, Michele Occhipinti, Andre Kuehne, Domokos Máthé, Noémi Kovács, Helmar Waiczies, Kjell Erlandsson, Debora Salvado, Marco Carminati, Giovanni L Montagnani, et al. Development of clinical simultaneous SPECT/MRI. *The British journal of radiology*, 91(1081):20160690, 2018.

[33] Abhinav Jha, Steven Rowe, Yong Du, and Eric Frey. An unsupervised semi-automated segmentation technique to delineate tumors and bones in SPECT images of patients with bone metastasis. *Journal of Nuclear Medicine*, 58(supplement 1):613–613, 2017.

[34] Abhinav K Jha, Brian Caffo, and Eric C Frey. A no-gold-standard technique for objective assessment of quantitative nuclear-medicine imaging methods. *Physics in Medicine & Biology*, 61(7):2780, 2016.

[35] Abhinav K Jha and Eric Frey. No-gold-standard evaluation of image-acquisition methods using patient data. In *Medical Imaging 2017: Image Perception, Observer Performance, and Technology Assessment*, volume 10136, page 101360L. International Society for Optics and Photonics, 2017.

[36] Abhinav K Jha, Matthew A Kupinski, Jeffrey J Rodriguez, Renu M Stephen, and Alison T Stopeck. Task-based evaluation of segmentation algorithms for diffusion-weighted MRI without using a gold standard. *Physics in Medicine & Biology*, 57(13):4425, 2012.

[37] Abhinav K Jha, Esther Mena, Brian S Caffo, Saeed Ashrafinia, Arman Rahmim, Eric C Frey, and Rathan M Subramaniam. Practical no-gold-standard evaluation framework for quantitative imaging methods: application to lesion segmentation in positron emission tomography. *Journal of Medical Imaging*, 4(1):011011, 2017.

[38] Abhinav K Jha, Jeffrey J Rodríguez, Renu M Stephen, and Alison T Stopeck. A clustering algorithm for liver lesion segmentation of diffusion-weighted MR images. In *2010 IEEE Southwest Symposium on Image Analysis & Interpretation (SSIAI)*, pages 93–96. IEEE, 2010.

[39] Abhinav K Jha, Na Song, Brian Caffo, and Eric C Frey. Objective evaluation of reconstruction methods for quantitative SPECT imaging in the absence of ground truth. In *Medical Imaging 2015: Image Perception, Observer Performance, and Technology Assessment*, volume 9416, page 94161K. International Society for Optics and Photonics, 2015.

[40] Merijn Joling, Chris Vriend, Odile A Van den Heuvel, Pieter GHM Raijmakers, Paul A Jones, Henk W Berendse, and Jan Booij. Analysis of extrastriatal 123I-FP-CIT binding contributes to the differential diagnosis of Parkinsonian diseases. *Journal of Nuclear Medicine*, 58(7):1117–1123, 2017.

[41] Konstantinos Kamnitsas, Christian Ledig, Virginia FJ Newcombe, Joanna P Simpson, Andrew D Kane, David K Menon, Daniel Rueckert, and Ben Glocker. Efficient multi-scale 3D CNN with fully connected CRF for accurate brain lesion segmentation. *Medical image analysis*, 36:61–78, 2017.

[42] Morvarid Karimi, LinLin Tian, Christopher A Brown, Hubert P Flores, Susan K Loftin, Tom O Videen, Stephen M Moerlein, and Joel S Perlmutter. Validation of nigrostriatal positron emission tomography measures: critical limits. *Annals of neurology*, 73(3):390–396, 2013.

[43] Michael Kass, Andrew Witkin, and Demetri Terzopoulos. Snakes: Active contour models. *International journal of computer vision*, 1(4):321–331, 1988.

[44] Ghazala Khan and Naimul Mefraz Khan. Brain MRI Segmentation using efficient 3D Fully Convolutional Neural Networks. In *2018 IEEE International Conference on Bioinformatics and Biomedicine (BIBM)*, pages 2351–2356. IEEE, 2018.

[45] Yun J Kim, Masanori Ichise, James R Ballinger, Douglas Vines, Sean S Erami, Tatsuro Tatschida, and Anthony E Lang. Combination of dopamine transporter and D2 receptor SPECT in the diagnostic evaluation of PD, MSA, and PSP. *Movement disorders: official journal of the Movement Disorder Society*, 17(2):303–312, 2002.

[46] Michael A King, David T Long, and A Bertrand Brill. SPECT volume quantitation: influence of spatial resolution, source size and shape, and voxel size. *Medical physics*, 18(5):1016–1024, 1991.

[47] Matthew A Kupinski, John W Hoppin, Eric Clarkson, Harrison H Barrett, and George A Kastis. Estimation in medical imaging without a gold standard. *Academic Radiology*, 9(3):290–297, 2002.

[48] Pamela J LaMontagne, Tammie L.S. Benzinger, John C. Morris, Sarah Keefe, Russ Hornbeck, Chengjie Xiong, Elizabeth Grant, Jason Hassenstab, Krista Moulder, Andrei Vlassenko, Marcus E. Raichle, Carlos Cruchaga, and Daniel Marcus. OASIS-3: Longitudinal Neuroimaging, Clinical, and Cognitive Dataset for Normal Aging and Alzheimer Disease. *medRxiv*, 2019.

[49] José L Lanciego, Natasha Luquin, and José A Obeso. Functional neuroanatomy of the basal ganglia. *Cold Spring Harbor perSPECTives in medicine*, 2(12):a009621, 2012.

[50] Anthony E Lang, Steven Gill, Nik K Patel, Andres Lozano, John G Nutt, Richard Penn, David J Brooks, Gary Hotton, Elena Moro, Peter Heywood, et al. Randomized controlled trial of intraputamenal glial cell line–derived neurotrophic factor infusion in Parkinson disease. *Annals of neurology*, 59(3):459–466, 2006.

[51] Kenneth Lange, Richard Carson, et al. EM reconstruction algorithms for emission and transmission tomography. *Journal of Computer Assisted Tomography*, 8(2):306–16, 1984.

[52] Jee-Young Lee, Nicholas P Lao-Kaim, Jacopo Pasquini, Günther Deuschl, Nicola Pavese, and Paola Piccini. Pallidal dopaminergic denervation and rest tremor in early Parkinson's disease: PPMI cohort analysis. *Parkinsonism & related disorders*, 51:101–104, 2018.

[53] Jee-Young Lee, Seongho Seo, Jae Sung Lee, Han-Joon Kim, Yu Kyeong Kim, and Beom S Jeon. Putaminal serotonergic innervation: monitoring dyskinesia risk in Parkinson disease. *Neurology*, 85(10):853–860, 2015.

[54] Kevin H Leung, Wael Marashdeh, Rick Wray, Saeed Ashrafinia, Martin G Pomper, Arman Rahmim, and Abhinav K Jha. A physics-guided modular deep-learning based automated framework for tumor segmentation in PET. *Physics in Medicine & Biology*, 2020.

[55] Geert Litjens, Thijs Kooi, Babak Ehteshami Bejnordi, Arnaud Arindra Adiyoso Setio, Francesco Ciompi, Mohsen Ghafoorian, Jeroen Awm Van Der Laak, Bram Van Ginneken, and Clara I Sánchez. A survey on deep learning in medical image analysis. *Medical image analysis*, 42:60–88, 2017.

[56] Jinxin Liu, Ziping Liu, Hae Sol Moon, Joyce Mhlanga, Barry Siegel, and Abhinav K. Jha. A no-gold-standard technique for objective evaluation of quantitative nuclear-medicine imaging methods in the presence of correlated noise. In *SNMMI Annual Meeting 2020*, accepted.

[57] Ziping Liu, Richard Laforest, Joyce Mhlanga, Hae Sol Moon, Tyler J Fraum, Malak Itani, Aaron Mintz, Farrokh Dehdashti, Barry A Siegel, and Abhinav K Jha. An estimation-based method to segment PET images. *arXiv preprint arXiv:2003.00317*, 2020.

[58] Ziping Liu, Hae Sol Moon, Joyce Mhlanga, , Barry Siegel, Richard Laforest, and Abhinav Jha. Fuzzy-SegNet: A fuzzy deep-learning-based automated segmentation method for PET images. In *WMIC 2019*, Montreal, Canada, Sept. 4-8 2019.

[59] Michael Ljungberg and Sven-Erik Strand. Attenuation and scatter correction in SPECT for sources in a nonhomogeneous object: a Monte Carlo study. *Journal of Nuclear Medicine*, 32(6):1278–1284, 1991.

[60] Nikos K Logothetis, Jon Pauls, Mark Augath, Torsten Trinath, and Axel Oeltermann. Neurophysiological investigation of the basis of the fMRI signal. *Nature*, 412(6843):150–157, 2001.

[61] David T Long, Michael A King, and John Sheehan. Comparative evaluation of image segmentation methods for volume quantitation in SPECT. *Medical physics*, 19(2):483–489, 1992.

[62] Francesca Magrinelli, Alessandro Picelli, Pierluigi Tocco, Angela Federico, Laura Roncari, Nicola Smania, Giampietro Zanette, and Stefano Tamburin. Pathophysiology of motor dysfunction in Parkinson's disease as the rationale for drug treatment and rehabilitation. *Parkinson's disease*, 2016, 2016.

[63] Panchanan Maiti, Jayeeta Manna, and Gary L Dunbar. Current understanding of the molecular mechanisms in Parkinson's disease: targets for potential treatments. *Translational neurodegeneration*, 6(1):28, 2017.

[64] Kenneth Marek, Danna Jennings, Shirley Lasch, Andrew Siderowf, Caroline Tanner, Tanya Simuni, Chris Coffey, Karl Kieburtz, Emily Flagg, Sohini Chowdhury, et al. The Parkinson progression marker initiative (PPMI). *Progress in neurobiology*, 95(4):629–635, 2011.

[65] FJ Martinez-Murcia, JM Górriz, J Ramírez, M Moreno-Caballero, M Gómez-Río, and Parkinson's Progression Markers Initiative. Parametrization of textural patterns in 123I-ioflupane imaging for the automatic detection of Parkinsonism. *Medical physics*, 41(1):012502, 2014.

[66] Manuela Matesan, Santhosh Gaddikeri, Katelan Longfellow, Robert Miyaoka, Saeed Elojeimy, Shana Elman, Shu-Ching Hu, Satoshi Minoshima, and David Lewis. I-123 DaTscan SPECT Brain Imaging in Parkinsonian Syndromes: Utility of the Putamen-to-Caudate Ratio. *Journal of Neuroimaging*, 28(6):629–634, 2018.

[67] Ross J McGurk, James Bowsher, John A Lee, and Shiva K Das. Combining multiple FDG-PET radiotherapy target segmentation methods to reduce the effect of variable performance of individual segmentation methods. *Medical physics*, 40(4):042501, 2013.

[68] M Mignotte, J Meunier, JP Soucy, and C Janicki. Segmentation and classification of brain SPECT images using 3D Markov random field and density mixture estimations. In *Proc. 5th World Multi-Conf. Systemics, Cybernetics and Informatics, Concepts and Applications of Systemics and Informatics*, volume 10, pages 239–244. Citeseer, 2001.

[69] Vishwesh Nath, Sudhir K Pathak, Kurt G Schilling, Walter Schneider, and Bennett A Landman. Deep learning estimation of multi-tissue constrained spherical deconvolution with limited single shell DW-MRI. In *Medical Imaging 2020: Image Processing*, volume 11313, page 113130S. International Society for Optics and Photonics, 2020.

[70] C Warren Olanow, Matthew B Stern, and Kapil Sethi. The scientific and clinical basis for the treatment of Parkinson disease (2009). *Neurology*, 72(21 Supplement 4):S1–S136, 2009.

[71] Giovanni Palermo and Roberto Ceravolo. Molecular Imaging of the Dopamine Transporter. *Cells*, 8(8):872, 2019.

[72] Eunkyung Park, Yu Mi Hwang, Chan-Nyoung Lee, Sujin Kim, Sun Young Oh, Young Chul Kim, Jae Gol Choe, and Kun Woo Park. Differential diagnosis of patients with inconclusive Parkinsonian features using [18 F] FP-CIT PET/CT. *Nuclear medicine and molecular imaging*, 48(2):106–113, 2014.

[73] Joel S Perlmutter and Scott A Norris. Neuroimaging biomarkers for Parkinson's disease: Facts and fantasy. *Annals of neurology*, 76(6):769–783, 2014.

[74] Ronald Carl Petersen, PS Aisen, Laurel A Beckett, MC Donohue, AC Gamst, Danielle J Harvey, CR Jack, WJ Jagust, LM Shaw, AW Toga, et al. Alzheimer's disease neuroimaging initiative (ADNI): clinical characterization. *Neurology*, 74(3):201–209, 2010.

[75] Michelle Porritt, Davor Stanic, David Finkelstein, Peter Batchelor, Sharon Lockhart, Andrew Hughes, Renate Kalnins, and David Howells. Dopaminergic innervation of the human striatum in Parkinson's disease. *Movement disorders: official journal of the Movement Disorder Society*, 20(7):810–818, 2005.

[76] R Prashanth, Sumantra Dutta Roy, Pravat K Mandal, and Shantanu Ghosh. High-accuracy classification of Parkinson's disease through shape analysis and surface fitting in 123I-Ioflupane SPECT imaging. *IEEE journal of biomedical and health informatics*, 21(3):794–802, 2016.

[77] Arman Rahmim, Yousef Salimpour, Saurabh Jain, Stephan AL Blinder, Ivan S Klyuzhin, Gwenn S Smith, Zoltan Mari, and Vesna Sossi. Application of texture analysis to DAT SPECT imaging: relationship to clinical assessments. *NeuroImage: Clinical*, 12:e1–e9, 2016.

[78] B Ravina, D Eidelberg, JE Ahlskog, RL Albin, DJ Brooks, M Carbon, V Dhawan, A Feigin, S Fahn, M Guttman, et al. The role of radiotracer imaging in Parkinson disease. *Neurology*, 64(2):208–215, 2005.

[79] Karen Suzanne Rommelfanger and Thomas Wichmann. Extrastriatal dopaminergic circuits of the basal ganglia. *Frontiers in neuroanatomy*, 4:139, 2010.

[80] Holger R Roth, Amal Farag, Le Lu, Evrim B Turkbey, and Ronald M Summers. Deep convolutional networks for pancreas segmentation in CT imaging. In *Medical Imaging 2015: Image Processing*, volume 9413, page 94131G. International Society for Optics and Photonics, 2015.

[81] Olivier G Rousset, Yilong Ma, Alan C Evans, et al. Correction for partial volume effects in PET: principle and validation. *Journal of Nuclear Medicine*, 39(5):904–911, 1998.

[82] Makoto Sasaki, Eri Shibata, Kohsuke Kudo, and Koujiro Tohyama. Neuromelanin-sensitive MRI. *Clinical Neuroradiology*, 18(3):147–153, 2008.

[83] Kimberly D Seifert and Jonathan I Wiener. The impact of DaTscan on the diagnosis and management of movement disorders: A retroSPECTive study. *American journal of neurodegenerative disease*, 2(1):29, 2013.

[84] Piotr J Slomka, Gilbert A Hurwitz, Grace St Clement, and Janice Stephenson. Three-dimensional demarcation of perfusion zones corresponding to specific coronary arteries: application for automated interpretation of myocardial SPECT. *Journal of Nuclear Medicine*, 36(11):2120–2126, 1995.

[85] Sharon Smaga. Tremor. *American family physician*, 68(8):1545–1552, 2003.

[86] James A Sorenson, Michael E Phelps, et al. *Physics in nuclear medicine*. Grune & Stratton New York, 1987.

[87] Marine Soret, Stephen L Bacharach, and Irene Buvat. Partial-volume effect in PET tumor imaging. *Journal of Nuclear Medicine*, 48(6):932–945, 2007.

[88] Maria Grazia Spillantini, R Anthony Crowther, Ross Jakes, Masato Hasegawa, and Michel Goedert. α-Synuclein in filamentous inclusions of Lewy bodies from Parkinson's disease and dementia with Lewy bodies. *Proceedings of the National Academy of Sciences*, 95(11):6469–6473, 1998.

[89] Roger T Staff, Trevor S Ahearn, Kevin Wilson, Carl E Counsell, Kate Taylor, Robert Caslake, Joyce E Davidson, Howard G Gemmell, and Alison D Murray. Shape analysis of 123I-N-ω-fluoropropyl-2-β-carbomethoxy-3β-(4-iodophenyl) nortropane single-photon emission computed tomography images in the assessment of patients with Parkinsonian syndromes. *Nuclear medicine communications*, 30(3):194–201, 2009.

[90] MK Stam, EE Verwer, J Booij, SM Adriaanse, CM de Bruin, and TC de Wit. Performance evaluation of a novel brain-dedicated SPECT system. *European journal of nuclear medicine and molecular imaging physics*, 5(1):1–14, 2018.

[91] Renu M Stephen, Abhinav K Jha, Denise J Roe, Theodore P Trouard, Jean-Philippe Galons, Matthew A Kupinski, Georgette Frey, Haiyan Cui, Scott Squire, Mark D Pagel, et al. Diffusion MRI with semi-automated segmentation can serve as a restricted predictive biomarker of the therapeutic response of liver metastasis. *Magnetic resonance imaging*, 33(10):1267–1273, 2015.

[92] Robert Z Stodilka, Brad J Kemp, Frank S Prato, and Richard L Nicholson. Importance of bone attenuation in brain SPECT quantification. *Journal of Nuclear Medicine*, 39(1):190–197, 1998.

[93] Jianjun Sun, Jinbin Xu, Nigel J Cairns, Joel S Perlmutter, and Robert H Mach. Dopamine D1, D2, D3 receptors, vesicular monoamine transporter type-2 (VMAT2) and dopamine transporter (DAT) densities in aged human brain. *PloS one*, 7(11):e49483, 2012.

[94] Samer D Tabbal, LinLin Tian, Morvarid Karimi, Christopher A Brown, Susan K Loftin, and Joel S Perlmutter. Low nigrostriatal reserve for motor Parkinsonism in nonhuman primates. *Experimental neurology*, 237(2):355–362, 2012.

[95] Abdel Aziz Taha and Allan Hanbury. Metrics for evaluating 3D medical image segmentation: analysis, selection, and tool. *BMC medical imaging*, 15(1):29, 2015.

[96] LinLin Tian, Morvarid Karimi, Susan K Loftin, Chris A Brown, HuChuan Xia, JinBin Xu, Robert H Mach, and Joel S Perlmutter. No differential regulation of dopamine transporter (DAT) and vesicular monoamine transporter 2 (VMAT2) binding in a primate model of Parkinson disease. *PLoS One*, 7(2), 2012.

[97] Masakazu Tsujimoto, Atsushi Teramoto, Seiichiro Ota, Hiroshi Toyama, and Hiroshi Fujita. Automated segmentation and detection of increased uptake regions in bone scintigraphy using SPECT/CT images. *Annals of nuclear medicine*, 32(3):182–190, 2018.

[98] Zuzana Walker, DC Costa, Rodney WH Walker, K Shaw, S Gacinovic, T Stevens, G Livingston, P Ince, IG McKeith, and CLE Katona. Differentiation of dementia with Lewy bodies from Alzheimer's disease using a dopaminergic presynaptic ligand. *Journal of Neurology, Neurosurgery & Psychiatry*, 73(2):134–140, 2002.

[99] Tonghe Wang, Yang Lei, Haipeng Tang, Zhuo He, Richard Castillo, Cheng Wang, Dianfu Li, Kristin Higgins, Tian Liu, Walter J Curran, et al. A learning-based automatic segmentation and quantification method on left ventricle in gated myocardial perfusion SPECT imaging: A feasibility study. *Journal of Nuclear Cardiology*, pages 1–12, 2019.

[100] Alan L Whone, Robert Y Moore, Paola P Piccini, and David J Brooks. Plasticity of the nigropallidal pathway in Parkinson's disease. *Annals of Neurology: Official Journal of the American Neurological Association and the Child Neurology Society*, 53(2):206–213, 2003.

[101] Alan L Whone, Ray L Watts, A Jon Stoessl, Margaret Davis, Sven Reske, Claude Nahmias, Anthony E Lang, Olivier Rascol, Maria J Ribeiro, Philippe Remy, et al. Slower progression of Parkinson's disease with ropinirole versus levodopa: the REAL-PET study. *Annals of neurology*, 54(1):93–101, 2003.

[102] Qihang Yu, Yingda Xia, Lingxi Xie, Elliot K Fishman, and Alan L Yuille. Thickened 2D Networks for 3D Medical Image Segmentation. *arXiv preprint arXiv:1904.01150*, 2019.

[103] Xiujuan Zheng, Wentao Wei, Qiu Huang, Shaoli Song, Jieqing Wan, and Gang Huang. A Computer-Aided Analysis Method of SPECT Brain Images for Quantitative Treatment Monitoring: Performance Evaluations and Clinical Applications. *BioMed research international*, 2017, 2017.

[104] Morten Ziebell, Lars H Pinborg, Gerda Thomsen, Robin de Nijs, Claus Svarer, Aase Wagner, and Gitte M Knudsen. MRI-guided region-of-interest delineation is comparable to manual delineation in dopamine transporter SPECT quantification in patients: a reproducibility study. *Journal of nuclear medicine technology*, 38(2):61–68, 2010.

[105] Alex P Zijdenbos, Benoit M Dawant, Richard A Margolin, and Andrew C Palmer. Morphometric analysis of white matter lesions in MR images: method and validation. *IEEE transactions on medical imaging*, 13(4):716–724, 1994.